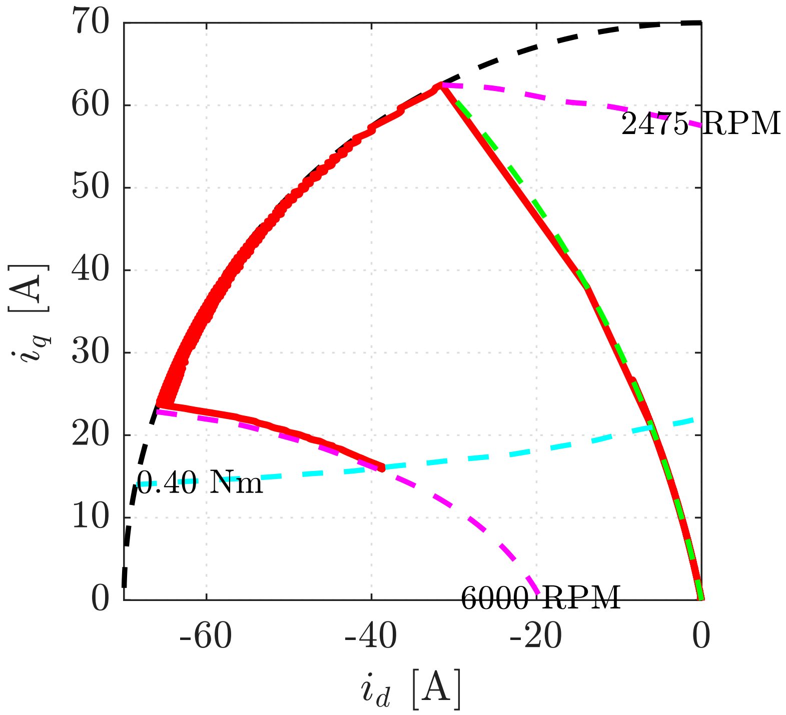

Mapping of a salient-pole PMSM and data-driven current vector selection

Development of an automated mapping system for PMSMs and evaluation of data-driven current selection

Master's thesis in Systems, Control and Mechatronics

Ivan Gunnarsson
William Nordkvist

DEPARTMENT OF ELECTRICAL ENGINEERING
CHALMERS UNIVERSITY OF TECHNOLOGY
Gothenburg, Sweden 2026
www.chalmers.se

Master's thesis 2026

Mapping of a salient-pole PMSM and data-driven current vector selection

Development of an automated mapping system for PMSMs and evaluation of data-driven current selection

IVAN GUNNARSSON
WILLIAM NORDKVIST

Department of Electrical Engineering
Division of Systems and Control
Chalmers University of Technology
Gothenburg, Sweden 2026

Mapping of a salient-pole PMSM and data-driven current vector selection
Development of an automated mapping system for PMSMs and evaluation of data-driven current selection
IVAN GUNNARSSON
WILLIAM NORDKVIST

© IVAN GUNNARSSON, WILLIAM NORDKVIST 2026.

Supervisors:
Daniel Chädström, Aros Electronics AB
Jimmy Björkman, Aros Electronics AB
Philip Axelsson, Aros Electronics AB
Examiner:
Stefan Lundberg, Department of Electrical Engineering

Master's Thesis 2026
Department of Electrical Engineering
Division of Systems and Control
Chalmers University of Technology
SE-412 96 Gothenburg
Telephone +46 31 772 1000

Cover: Current reference trajectory in the *dq*-plane during acceleration test.

Typeset in LaTeX
Printed by Chalmers Reproservice
Gothenburg, Sweden 2026

Mapping of a salient-pole PMSM and data-driven current vector selection
Development of an automated mapping system for PMSMs and evaluation of data-driven current selection
Ivan Gunnarsson
William Nordkvist
Department of Electrical Engineering
Chalmers University of Technology

Abstract

Efficient operation of Permanent Magnet Synchronous Machines (PMSMs) requires accurate knowledge of the machine's behaviour. Conventional control strategies often rely on linear machine models with constant parameters, which do not capture non-linear effects such as magnetic saturation, cross-saturation, speed-dependent losses, and temperature-dependent parameter variations. This thesis presents the development of an automated experimental mapping system for a salient-pole PMSM and investigates how measured machine data can be used for data-driven current vector selection.

The automated mapping system was developed to gather data about machine behaviour through systematic measurements performed in a machine test bench. Measurements of currents, voltages and produced torque were collected at different speeds and temperatures. The data was used to investigate how the true machine behaviour deviates from the linear model. This was done using visualizations of torque surfaces, flux-linkage and efficiency maps and voltage ellipses compared for different speed and temperature conditions. The largest deviations from the linear model could be explained by magnetic saturation and cross saturation at large current magnitudes, noticeable both in the torque and voltage behaviour. Within the investigated operating region, the calculated inductances based on the measurements showed that the values of L_d and L_q could vary up to 50 % and 60 % respectively compared to the linear model, while the cross inductances L_{dq} and L_{qd} had absolute values up to 0.04 mH and 0.03 mH respectively.

The mapped machine behaviour was used to develop a model for simulation in Simulink using Look-up Tables (LUT) for flux linkage and torque. Steady-state validation of the model yielded high accuracy for the case used in table generation 2000 RPM and 50 °C, achieving mean current errors below 0.5 A and a mean torque error of 0.087 Nm, largely attributed to the introduced zero-torque compensation. The simulation model was used to evaluate a control method that utilizes LUTs to provide current references based on the given torque demand, as well as voltage and current limitations. While having some numerical instabilities, the developed current vector selector proved to be a valid approach, handling several limitation cases effectively while the voltage utilization is held accurately at 95 % as limited by the control implementation. Furthermore, using mapped data to implement a Maximum Torque Per Watt trajectory yielded a mean machine efficiency of 65.26 %, corresponding to a 0.21 % increase compared to a mapped MTPA strategy.

Keywords: Electric drive system, Field-weakening control, Data-driven current selection, Experimental mapping, Look-up table

Acknowledgements

Firstly, we would like to thank our supervisors, Daniel Chädström, Jimmy Björkman and Philip Axelsson at Aros Electronics for their valuable advice and many interesting discussions. We would also like to thank all other coworkers at Aros Electronics that have shown interest in our project and helped us along the way. A special thanks also goes to our examiner Stefan Lundberg for his guidance during this spring.

Ivan Gunnarsson & William Nordkvist, Gothenburg, June 2026

List of Acronyms

Below is the list of acronyms that have been used throughout this thesis listed in alphabetical order:

AC	Alternating Current
ADC	Analogue to Digital Converter
back-EMF	Back Electromotive Force
CAN	Controller Area Network
CPU	Central Processing Unit
DC	Direct Current
dq-frame	Direct-Quadrature coordinate frame
FOC	Field-Oriented Control
GIL	Global Interpreter Lock
LUT	Look-Up Table
MCU	Microcontroller Unit
MOSFET	Metal-Oxide-Semiconductor Field-Effect Transistor
MTPA	Maximum Torque Per Ampere
MTPV	Maximum Torque Per Volt
MTPW	Maximum Torque Per Watt
NdFeB	Neodymium-Iron-Boron
PI	Proportional-Integral
PMSM	Permanent Magnet Synchronous Machine
PWM	Pulse Width Modulation
RBF	Radial Basis Function
RPM	Revolutions Per Minute
SVPWM	Space Vector Pulse Width Modulation
VSI	Voltage Source Inverter

Nomenclature

Below is the nomenclature of indices, sets, parameters, and variables that have been used throughout this thesis.

Parameters

i	Electrical current
i_a, i_b, i_c	Phase currents
i_d	Direct-axis current component in the dq-frame
i_q	Quadrature-axis current component in the dq-frame
$i_{d,avg}$	Averaged direct-axis current component
$i_{q,avg}$	Averaged quadrature-axis current component
$i_{d,ref}$	Direct-axis current reference
$i_{q,ref}$	Quadrature-axis current reference
$i_{d,tol}$	Direct-axis current tolerance
$i_{q,tol}$	Quadrature-axis current tolerance
$i_{enclosed}$	Current enclosed by integration path
i_x	Current in phase x
H	Magnetic field strength
B	Magnetic flux density
B_m	Maximum magnetic flux density
μ	Permeability
Φ	Magnetic flux
Ψ	Flux linkage
Ψ_a	Flux linkage in phase a
Ψ_d	Direct-axis flux linkage
Ψ_q	Quadrature-axis flux linkage
Ψ_m	Permanent magnet flux linkage

Ψ_{12}	Flux linkage in winding 2 caused by current in winding 1
I	Current magnitude
I_1	Current in winding 1
I_{dq}	Current magnitude in the dq-frame
$I_{dq,max}$	Maximum current magnitude in the dq-frame
ω	Electrical rotational speed
Ω	Mechanical rotational speed
Ω_{ref}	Mechanical speed reference
Ω_{tol}	Mechanical speed tolerance
t	Time
t_d	Dead time
N	Number of turns in windings
e	Induced voltage
e_a	Induced voltage in phase a
F	Force
R_m	Reluctance
l	Magnetic path length
A	Cross-sectional area
p	Number of pole pairs
θ	Electrical angle
Θ	Mechanical angle
s	General variable
s_a, s_b, s_c	General phase quantities
s_α, s_β	General quantities in the $\alpha\beta$-frame
s_d, s_q	General quantities in the dq-frame
a, b, c	Phase notation
K	Scaling constant for Clarke coordinate transform
L	Inductance
L_d	Direct-axis inductance
L_q	Quadrature-axis inductance
L_{dq}	Cross inductance from the q-axis to the d-axis
L_{qd}	Cross inductance from the d-axis to the q-axis
L_{12}	Cross inductance from winding 1 to winding 2
u	Voltage

u_a, u_b, u_c	Phase voltages
u_d	Direct-axis voltage component
u_q	Quadrature-axis voltage component
u_{DS}	Voltage drop over conducting MOSFET
U_{dc}	DC-link voltage
$U_{dq,max}$	Maximum voltage magnitude in the dq-frame
U_F	Diode forward voltage
Δu_x	Average voltage error in phase x
k_u	Voltage utilization
R	Resistance
R_0	Resistance at reference temperature
R_s	Stator phase resistance
$R_{DS(on)}$	MOSFET on-state resistance
T	Torque or temperature, depending on context
T_0	Reference temperature
T_e	Electromagnetic torque
T_s	Stator temperature
$T_{s,ref}$	Stator temperature reference
$\dot{T}_{tol}$	Maximum allowed torque derivative for steady-state detection
P	Power
P_e	Electrical power
P_m	Mechanical power
P_{Cu}	Copper loss power
P_{Fe}	Iron loss power
η	Machine efficiency
f	Frequency
f_{sw}	Switching frequency
β	Current vector angle from the positive d-axis
β_{MTPA}	Current vector angle for the MTPA trajectory
k	Sample index or constant, depending on context
k_{MTPA}	Linear constant in MTPA approximation
k_p	Proportional gain
k_i	Integral gain
k_h	Hysteresis loss coefficient

k_d	Eddy-current loss coefficient
k_e	Excess loss coefficient
x	Sample value
x_{accu}	Accumulated sample value
x_{avg}	Averaged sample value
n	Number of accumulated samples
m	Moving-average window size
W	Window length used for steady-state detection
α_{cu}	Temperature coefficient of copper resistance

Contents

List of Figures

List of Tables

1

Introduction

1.1 Background

Electric drive systems play a central role in modern energy consumption across all sectors of society. In 2023, electric motor systems accounted for 53% of the global electricity consumption. The largest sectors being industry, buildings, transport and agriculture, where the total electricity consumption by electric motors reached 13 467 TWh [1]. With electricity generation producing around 13 900 million tonnes of carbon dioxide per year, it is the largest source of energy-related emissions [2]. It is therefore crucial to ensure that electric drive systems operate as efficiently as possible to minimize their energy consumption and thereby minimize the associated carbon dioxide emissions.

Improving the efficiency of an electric drive system is often challenging from a hardware perspective. Redesigned machine geometries, improved materials or more advanced power electronics typically involve high costs and significant development [3]. As a result, it is important to optimize the control strategies of the existing hardware. By improving the utilization of the machine through enhanced control methods, efficiency gains can be achieved without physical modifications to the drive system.

Permanent Magnet Synhronous Machines (PMSM) are widely used in high-performance electric drive systems, such as electric vehicles and industrial applications, due to their high efficiency and high torque density over a wide operating range [4]. In a PMSM, the permanent magnets are responsible for the magnetic field produced in the rotor, which reduces losses that other machine types have that require external excitation for the rotor field. Additionally, a salient pole PMSM has a rotor structure that causes the magnetic field produced by the stator to behave differently depending on the rotor position. This means that the machine can produce torque in more than one way, both from the permanent magnets and from the geometry of the rotor, giving an additional degree of freedom in the control system [5]. The control system must therefore choose how the stator currents are applied to the machine depending torque requirement, current limitation and voltage limitation. This choice is important because a well selected current vector can reduce losses, improve efficiency and increase the operating range of the machine [6].

A common approach when modelling and controlling PMSMs is to use a linear model where the three-phase AC currents and voltages are transformed into the *dq*-frame, where AC quantities can be expressed as DC quantities in steady state [5]. This model does assume that the parameters, like inductances, resistance and permanent magnet flux linkage, are constant. In real machines, iron losses, magnetic saturation, cross-inductance effects and temperature dependant parameter variations lead to non-linear behaviour that deviates from the assumed model [7].

These model deviations can become especially important when the machine is operated close to its current and voltage limits, where accurate prediction of torque and voltage is necessary to select a suitable current vector. If the controller relies on a simplified model that does not represent the real machine behaviour, the selected operating point may lead to higher losses, reduced torque capability or limited field-weakening performance. One way to reduce this uncertainty is to experimentally map the machine over the relevant operating range and use the measured relationships between current, voltage and torque for a data-driven model.

1.2 Aim

The aim of this project is to experimentally determine the characteristics of a salient-pole PMSM over a wide range of operating points and investigate where the real machine behaviour deviates from the conventional linear model. In order to efficiently perform measurements and ensure consistency, a measurement script will be developed. The script will collect a comprehensive experimental dataset of voltages, torque and currents at different speeds and temperatures. From the mapped dataset, visualizations of voltage ellipses, torque maps, flux linkages and parameter variations in the *dq*-plane will be used to compare the true machine behaviour to the linear model.

The experimental mapping will be used to develop a data-driven machine model for simulation, allowing the measured behaviour of the machine to be represented more realistically. Based on the mapped data, an alternative approach to selecting the current vector reference will be investigated through simulations using the constructed machine model.

1.3 Scope

This project will handle one specific salient-pole PMSM and no other type of electrical machines. Although the methodology developed in this project should be applicable to any electric machine that uses Field Oriented Control (FOC), the experimental testing and validation will only be carried out on a single machine, thus the results will be specific to that machine.

The focus of this project is the conversion between the requested torque and current references needed to provide that torque at steady-state operation. The transient behaviour of the currents will not be addressed and the parameters of the current regulator will not be adjusted based on the machine's operating point. The current regulators and speed regulator have been tuned to have stable step responses across the operating range of the machine.

With the unidirectional power supply and inverter used for this project, the experimental work was limited to motor operation. Allowing only measurements to be made in the upper half of the *dq*-plane. However, the method was developed such that the whole *dq*-plane could be considered with the use of bidirectional power supply and inverter.

2

The Electric Drive System

The purpose of an electric drive system is to control the conversion between electrical power and mechanical power. In motor operation, the electric power from the power supply is transformed to mechanical power by the electric machine and is consumed by a mechanical load. In this case the machine is often referred to as a motor. If the power flow is instead going the opposite direction, mechanical power is transformed to electrical power by the machine to be consumed by an electrical load, the machine is referred to as a generator. A power electronic converter is used between the power supply and the electric machine to adapt the voltage, current and frequency to match the specifications of the supply and machine. A controller uses information about the system from sensors to control the power flow in the system.

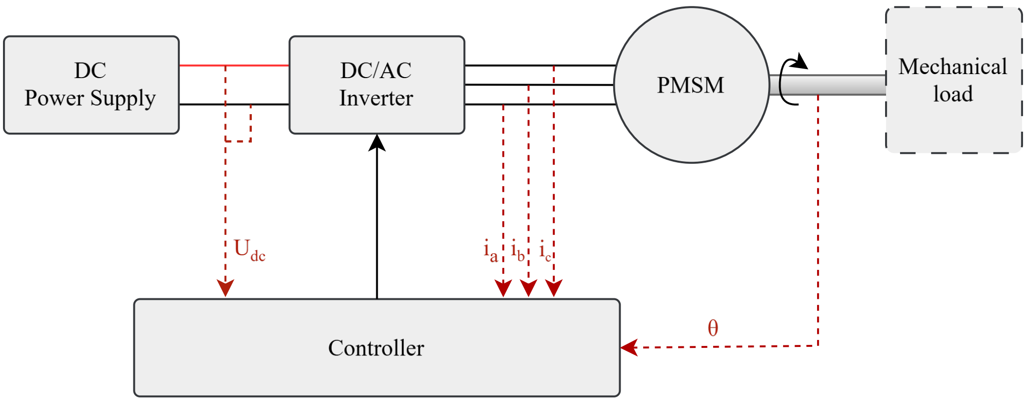

Figure 2.1: Schematic of the electric drive system

The electric drive system used in this project, illustrated in Figure 2.1, uses a DC power supply and a DC/AC inverter to drive a salient-pole PMSM. The DC power supply is unidirectional, meaning that it can only supply power and not act as a load, limiting the drive system to motor operation. The controller that is used to control the inverter has access to measurements of the DC voltage from the power supply and the phase currents to the machine along with the rotor angle from an encoder on the machine shaft. The mechanical load in Figure 2.1 represents the system connected to the machine shaft. In the following sections the salient-pole PMSM, inverter and control system will be further explained in detail.

2.1 Salient-pole PMSM

A Permanent Magnet Synchronous Machine (PMSM) is a type of AC machine where the magnetic field produced by the rotor is created by permanent magnets. The stationary part of the machine is called stator and contains an iron core with three-phase windings placed in slots. The rotating part of the machine, surrounded by the stator for an inrunner machine, is called rotor and contains the permanent magnets, rotor iron and the shaft. Between the rotor and the stator there is a small air gap which allows the rotor to rotate while still allowing magnetic interaction between the stator and rotor fields.

The operation of a PMSM is based on the fundamental laws of electromagnetism. When current flows through the stator windings, a magnetic field is produced around the conductors according to Ampere's law. In simplified form, it can be written as [8],

$$\oint H dl = i_{enclosed} \tag{2.1}$$

where H is the magnetic field strength and $i_{enclosed}$ is the current enclosed by the integration path. The magnetic field strength is related to the magnetic flux density according to,

$$B = \mu H \tag{2.2}$$

where B is the magnetic flux density and μ is the permeability of the material. The magnetic flux density flowing through a surface is the magnetic flux, denoted Φ. For a winding with several turns, the total flux linkage can be written as [9],

$$\Psi = N\Phi \tag{2.3}$$

where Ψ is the flux linkage and N is the number of turns in the winding.

When the three stator phases are supplied with sinusoidal currents that are shifted 120 electrical degrees, the resulting magnetic field rotates around the air gap. The three-phase stator currents can be written as,

$$i_a = I\cos(\omega t) \tag{2.4}$$
$$i_b = I\cos(\omega t + 2\pi/3) \tag{2.5}$$
$$i_c = I\cos(\omega t + 4\pi/3) \tag{2.6}$$

where I is the current amplitude and ω is the electrical angular frequency and each phase is shifted by 120 electrical degrees. These currents create a magnetic field, according to (2.1), that rotates around the rotor due to the sinusoidal AC current and the phase shift between phases. The magnetic field created by the stator windings then interacts with the magnetic field from the rotor permanent magnets.

In a PMSM, the magnetic flux that passes through the rotor iron, crosses the air gap, enters the stator iron, and links with the stator windings is denoted Ψ_m, called the permanent magnet flux linkage. When the rotor rotates, the permanent magnet flux linkage for each stator phase varies with time, causing a voltage over the windings according to Faraday's law [8],

$$e = -\frac{d\Psi}{dt} \tag{2.7}$$

where e is the induced voltage. And for a specific phase, the induced voltage, caused by the permanent magnets, will depend on the rotor angle,

$$e_a = -\frac{d\Psi_a}{dt} = -\frac{d\Psi_m \cos(\theta)}{dt} \tag{2.8}$$

where θ is the rotor angle from stator phase a. This induced voltage is referred to as the back Electromotive Force (back-EMF) during motor operation. The same principle also explains generator operation, where mechanical rotation of the rotor causes the permanent magnet flux linkage in the stator windings to vary with time, thereby producing an induced voltage.

Torque is produced by the interaction in the air gap between the magnetic field created by the stator currents and the magnetic field created by the permanent magnets in the rotor. When these two fields are not aligned, electromagnetic forces are produced which act tangentially around the air gap and create torque on the rotor. This force production can be described by the Lorentz force law [8],

$$F = il \times B \tag{2.9}$$

where F is the force acting on a current-carrying conductor, i is the current, l is a vector in the direction of the conductor. The resulting forces act on the stator and rotor with equal magnitude and opposite direction, and the reaction torque causes the rotor to rotate.

The torque production can also be understood from the tendency of magnetic fields to align. A magnetic system tends to move toward a position where the magnetic energy is minimized, where the opposite poles on the stator and rotor are aligned [10]. Therefore, if the stator magnetic field is placed at an angle relative to the permanent magnet field, the rotor will experience a torque that tries to align the fields. For continuous rotation with constant torque, the stator field must rotate ahead of the rotor field such that the rotor is continuously pulled forward. This results in the rotor rotating synchronously with the rotating magnetic field produced by the stator in steady-state operation, hence the name synchronous machine [9].

For maximum torque production from the permanent magnet field, the stator field produced by the stator currents should ideally be oriented perpendicular to the rotor permanent magnet field. If the fields are aligned, the magnetic attraction is strong but the tangential force component is small, so little or no useful torque is produced. If the stator field is 90 electrical degrees from the rotor permanent magnet field, the tangential force component is maximized, which gives high torque production [10].

For salient-pole PMSMs, an additional torque component is caused by differences in the magnetic properties of the rotor in different directions. Due to the rotor iron geometry and the placement of the permanent magnets, the magnetic path through the rotor depends on the orientation of the stator field relative to the rotor. This means that the magnetic reluctance is not the same in all directions. Magnetic reluctance describes how much a magnetic path opposes magnetic flux and can be written as [8],

$$R_m = \frac{l}{\mu A} \tag{2.10}$$

where R_m is the reluctance, l is the magnetic path length, μ is the permeability of the material, and A is the cross-sectional area of the magnetic path. The difference in reluctance is what defines a salient-pole PMSM, compared to a PMSM with non-salient poles, where the reluctance is constant.

Since the reluctance depends on direction, the flux linkage produced by the stator currents also depends on the angle between the stator field and the rotor. If the stator field is aligned with a direction of low reluctance, the same current produces a larger flux linkage than if it is aligned with a direction of high reluctance. When the stator field is placed between these two directions, the rotor experiences a torque that tries to align the low-reluctance rotor direction with the stator field. This torque is produced because such an alignment increases the flux linkage for the same current and reduces the magnetic energy stored in the air gap [10]. The reluctance torque is zero when the stator field is aligned exactly with either the low-reluctance or high-reluctance direction, since there is then no preferred direction for further rotation. The reluctance torque is maximized when the stator field is placed between the two magnetic axes, because this is where a small change in rotor position gives the largest change in magnetic energy and flux linkage.

For a synchronous machine the electrical frequency and mechanical frequency is related through the number of pole pairs. One pole pair consists of one north and one south pole on the rotor. If a machine has p pole pairs, then one mechanical revolution is equal to p electrical revolutions. This results in the following relations for rotor angle and angular velocity [9],

$$\theta = p\Theta \tag{2.11}$$

$$\omega = p\Omega \tag{2.12}$$

where θ is the electrical angle, Θ is the mechanical angle, ω is the electrical angular velocity, Ω is the mechanical angular velocity.

In Figure 2.2, a simplified cross-sectional layout of the salient-pole PMSM used in this project is shown. It has two pole pairs that are inserted in the iron core, where one of the pole pairs are visible in the figure. Since magnets have much lower permeability than the iron core, the reluctance will be higher in the direction of the magnets according to (2.10). This causes the rotor to have salient poles. Further the cross section shows the stator teeth that the windings are placed around, the small air gap between the stator and rotor and a place for the shaft to be inserted in the rotor.

In order to model the electromagnetic properties of the salient-pole PMSM and use them in the control system, the three-phase electrical quantities must first be

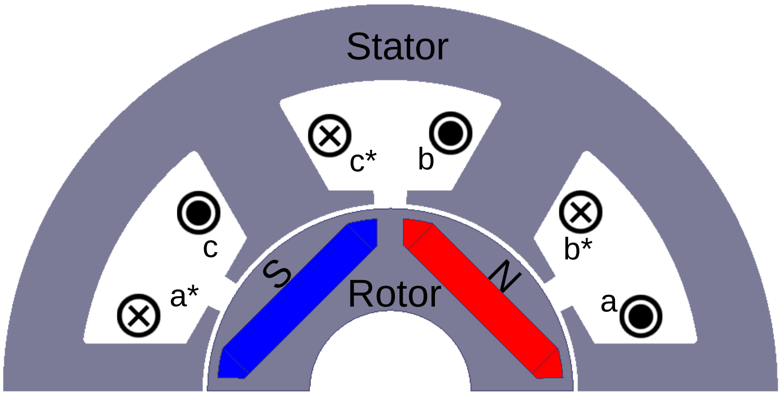

Figure 2.2: Simplified cross-sectional layout of the salient-pole PMSM.

expressed in a more convenient form. The next section therefore presents the Clarke and Park coordinate transformations, followed by the linear model of the salient-pole PMSM.

2.1.1 Clarke and Park coordinate transforms

To simplify the analysis and control of three-phase systems, coordinate transformations are commonly used. Instead of describing the machine using the three phase quantities directly, the same system can be represented using two equivalent components. In this section, the general variable s is used to represent a phase quantity, such as current, voltage or flux linkage.

The Clarke transform maps three-phase quantities into a stationary two axis reference frame, usually referred to as the $\alpha\beta$-system. This can be written as [9],

$$\begin{bmatrix} s_\alpha \\ s_\beta \end{bmatrix} = K \begin{bmatrix} \frac{2}{3} & -\frac{1}{3} & -\frac{1}{3} \\ 0 & \frac{1}{\sqrt{3}} & -\frac{1}{\sqrt{3}} \end{bmatrix} \begin{bmatrix} s_a \\ s_b \\ s_c \end{bmatrix} \tag{2.13}$$

where s_a, s_b and s_c are the three-phase quantities, s_α and s_β are equivalent quantities in the $\alpha\beta$-system, and K is a scaling constant. In this work, the scaling constant is chosen for power-invariant scaling, $K = \sqrt{3/2}$. This transformation is possible under the assumption that there is no zero sequence present in the three-phase system. In other words, the sum of all three phases equal zero, hence if two phase quantities are known, the third can be calculated. The Clarke transform is visualized in Figure 2.3.

The Park transform applies a rotation to the stationary $\alpha\beta$-system into a reference frame that rotates with the rotor of the machine. The rotating reference frame is commonly referred to as the dq-system. In this work, the direct axis (d-axis) of the rotating frame is aligned with the permanent magnet flux of the rotor. The quadrature axis (q-axis) is perpendicular to the d-axis and located 90 electrical degrees ahead in the direction of the rotation.

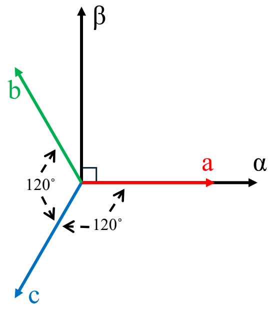

Figure 2.3: The direction of the three-phase components separated by 120° in the $\alpha\beta$-frame. The α-axis is aligned with phase a, while the β-axis is orthogonal to it.

The Park transformation is written as [9],

$$\begin{bmatrix} s_d \\ s_q \end{bmatrix} = \begin{bmatrix} \cos\theta & \sin\theta \\ -\sin\theta & \cos\theta \end{bmatrix} \begin{bmatrix} s_\alpha \\ s_\beta \end{bmatrix} \tag{2.14}$$

where s_d and s_q are the components in the rotating dq-system and θ is the angle between the stationary α-axis and the rotating d-axis. The Park transform is visualized in Figure 2.4.

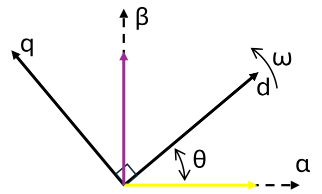

Figure 2.4: The α- and β-axis components in the $\alpha\beta$-frame and a rotating dq-frame. θ is the angle between the α- and d-axis, and ω is the angular velocity that the dq-frame rotates with.

The main advantage of the Clarke and Park transforms is that sinusoidal three-phase quantities become constant in steady-state operation when observed from the rotating dq-frame. This simplifies both analysis and control of the PMSM. Instead of controlling sinusoidal phase currents directly, the controller can regulate the d- and q-axis current components as DC quantities. This is the basis for Field-Oriented Control (FOC) which is commonly used for PMSM drive systems.

2.1.2 Linear model of the salient pole PMSM

The electromagnetic theory described in the previous sections explains how the PMSM operates physically. The permanent magnets create a flux linkage in the stator windings, the stator currents create their own magnetic field according to Ampere's law, and voltage is induced when the flux linkage changes with time according to Faraday's law. To use these effects in analysis and control, the machine is described by a mathematical model in the rotating dq-reference frame.

For the linear model, the magnetic circuit is assumed to be linear. The stator resistance and inductances are assumed constant, and the permanent magnet flux linkage is assumed to have constant magnitude. Under these assumptions, the flux linkages in the d- and q-axes can be written as [8],

$$\Psi_d = L_d i_d + \Psi_m \tag{2.15}$$
$$\Psi_q = L_q i_q \tag{2.16}$$

where i_d and i_q are the stator current components in the rotating dq-frame, L_d and L_q are the d- and q-axis inductances, and Ψ_m is the flux linkage produced by the permanent magnets. Since the d-axis is aligned with the permanent magnet flux, the permanent magnet flux linkage appears only in the d-axis equation. The q-axis flux linkage is therefore only produced by the q-axis current in this model.

The stator voltage equations can be obtained from the winding voltage relation, where the applied voltage must overcome the resistive voltage drop and the time variation of flux linkage. In the dq-frame, the rotation of the reference frame also introduces speed-dependent coupling terms between the axes. The PMSM voltage equations are [9],

$$u_d = R_s i_d + \frac{d\Psi_d}{dt} - \omega \Psi_q \tag{2.17}$$
$$u_q = R_s i_q + \frac{d\Psi_q}{dt} + \omega \Psi_d \tag{2.18}$$

where u_d and u_q are the d- and q-axis voltages, R_s is the stator phase resistance, and ω is the electrical angular velocity. The terms $R_s i_d$ and $R_s i_q$ describe the voltage drop over the resistance in the copper wire in the windings. The derivative terms describe voltage induced by changes in flux linkage, following Faraday's law. The terms $-\omega\Psi_q$ and $\omega\Psi_d$ appear because the dq-reference frame rotates with the rotor. These terms describe how flux linkage in one axis induces voltage in the other axis when the rotor is rotating. By inserting the linear flux linkage equations into the voltage equations, the linear dq-voltage model becomes,

$$u_d = R_s i_d + L_d \frac{di_d}{dt} - \omega L_q i_q \tag{2.19}$$
$$u_q = R_s i_q + L_q \frac{di_q}{dt} + \omega L_d i_d + \omega \Psi_m. \tag{2.20}$$

The term $\omega\Psi_m$ in the q-axis voltage equation is the back-EMF caused by the permanent magnet flux linkage. At steady-state, the time derivatives of the currents become zero.

The electromagnetic torque can be expressed using the d and q current components and flux linkages as [9],

$$T_e = \frac{3}{2K^2} p \left(\Psi_d i_q - \Psi_q i_d\right) \tag{2.21}$$

where T_e is the electromagnetic torque, K is the scaling used for the Clarke transform and p is the number of pole pairs. With power-invariant scaling, the term $\frac{3}{2K^2}$

becomes 1. By inserting the linear flux linkage expressions, the torque equation becomes,

$$T_e = p\left(\Psi_m i_q + \left(L_d - L_q\right) i_d i_q\right). \tag{2.22}$$

The first term is the permanent magnet torque. It is produced by the interaction between the q-axis current and the permanent magnet flux linkage. This corresponds to the torque production described earlier, where the stator field is oriented perpendicular to the rotor permanent magnet field to produce tangential force in the air gap.

The second term is the reluctance torque. It is only present when L_d and L_q are different, which is the case for a salient-pole PMSM. This term comes from the direction-dependent magnetic reluctance of the rotor. The reluctance torque depends on both i_d and i_q, which means that the current angle affects how much of the total torque comes from rotor saliency. For a non-salient PMSM, where $L_d = L_q$, this term becomes zero.

2.1.3 Efficiency of electric machines

The efficiency of an electric machine can be described as the ratio between the power put into the machine to the power taken out of the machine. If the machine is in motor operation, this would be the ratio between the electrical input power to the mechanical output power. Since power invariant scaling is used, the electrical power can be written as [9],

$$P_e = i_d u_d + i_q u_q \tag{2.23}$$

in the dq-reference frame. The mechanical power of the machine is,

$$P_m = T_e \Omega \tag{2.24}$$

where Ω is the mechanical rotational speed. Consequently, the efficiency of the machine in motor operation can be expressed as,

$$\eta = \frac{P_m}{P_e} = \frac{T_e \Omega}{i_d u_d + i_q u_q} \tag{2.25}$$

In case of generator operation, mechanical power is put into the system, while electrical power is taken out. The ratio describing efficiency would thus be inverted.

2.2 Inverter

The inverter is the power electronic converter placed between the DC power supply and the PMSM. Its purpose is to convert the DC-link voltage from the power supply into a three-phase AC voltage applied to the stator windings of the machine. In the drive system used in this project, the inverter is a three-phase Voltage Source Inverter (VSI). This means that the inverter is supplied from a relatively stiff DC voltage source and controls the machine phase voltages by switching the machine terminals between the positive and negative sides of the DC-link [9].

The inverter consists of three inverter legs, one for each phase. In Figure 2.5, a diagram of the three-phase inverter is shown. Each inverter leg is a half-bridge between the positive and negative side of the DC-link, with one of the machine phases connected to the middle point of the half-bridge. The switches that connect the machine phases to either the positive or negative side of the DC-link are Metal-Oxide-Semiconductor Field-Effect Transistors (MOSFET). The MOSFETs are controlled by the controller through gate drivers such that the desired voltage is applied to each phase.

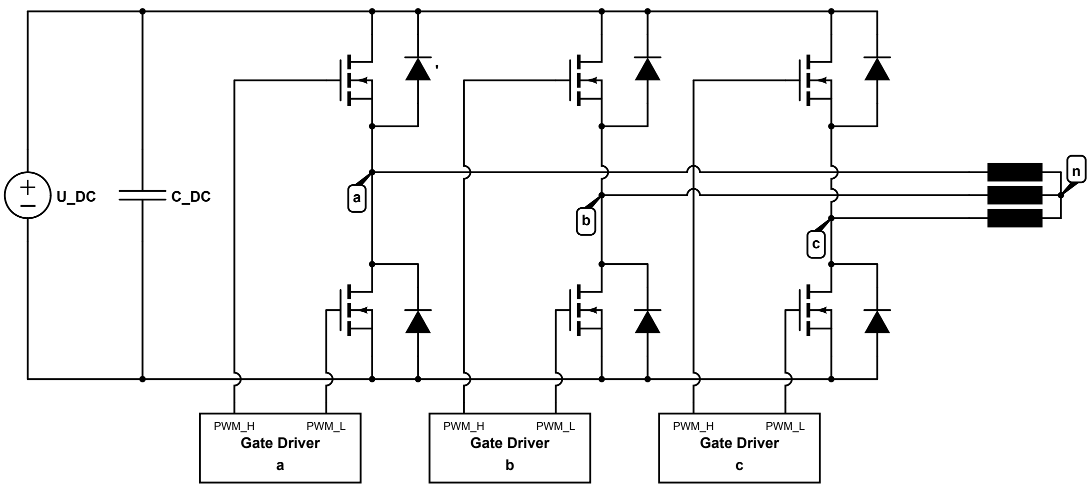

Figure 2.5: Schematic of a three-phase VSI supplied by a DC-link voltage U_{DC} and powering a three-phase load.

Since the inverter can only connect each phase terminal to discrete DC-link levels, it cannot generate a sinusoidal voltage directly. Instead, Pulse Width Modulation (PWM) is used. With PWM, the MOSFETs are switched at a high frequency and the duty cycle is varied such that the average voltage over one switching period corresponds to the desired voltage reference. The proportion of time per PWM period that a phase is connected to the positive side of the DC-link is called duty cycle. The machine windings act as an inductive filter, which makes the phase currents smoother than the switched phase voltages [9].

In this project, Space Vector Pulse Width Modulation, SVPWM, is used. SVPWM represents the three-phase inverter voltage as a voltage vector in the stationary $\alpha\beta$-plane. A two-level three-phase inverter has eight possible switching states. Six of these produce active voltage vectors and two produce zero voltage vectors. During each switching period, SVPWM applies the two active vectors closest to the desired reference vector, together with one or both zero vectors [11]. By choosing the time spent in each switching state, the average voltage vector over the switching period is made equal to the requested voltage vector.

The maximum voltage that can be applied to the PMSM is limited by the DC-link voltage. In the linear modulation range of SVPWM, the maximum voltage magnitude in the dq-plane, using power-invariant scaling, is [9],

$$U_{dq,\max} = \frac{U_{dc}}{\sqrt{2}} \tag{2.26}$$

where U_{dc} is the DC-link voltage. The voltage reference from the current controller must therefore satisfy the following inequality,

$$\sqrt{u_d^2 + u_q^2} \leq U_{dq,\max} \tag{2.27}$$

and the voltage utilization can be expressed as,

$$k_u = \frac{\sqrt{u_d^2 + u_q^2}}{U_{dq,\max}}. \tag{2.28}$$

In practice, the voltage applied by the inverter is not exactly equal to the reference voltage from the controller. One important reason is dead time [12]. The upper and lower MOSFETs in the same inverter leg must not conduct at the same time, since this would short-circuit the DC-link. Therefore, a short delay is inserted between turning one MOSFET off and turning the other MOSFET on. During this time both MOSFETs are off, but due to the inductance in the windings the phase current will continue to flow. Each MOSFET has a body diode that is connected in antiparallel where the currents can continue to flow even if both MOSFETs are off.

The dead time causes an error between the commanded and applied phase voltage. A simplified expression for the average voltage error in one phase is [12],

$$\Delta u_x \approx -\operatorname{sgn}(i_x) U_{dc} t_d f_{sw} \tag{2.29}$$

where i_x is the phase current, t_d is the dead time and f_{sw} is the switching frequency. The sign of the voltage error depends on the current direction, which can cause distortion of the phase voltages and currents.

Additional voltage errors are caused by the voltage drops in the conducting semiconductor devices. When a MOSFET conducts, the voltage drop can approximately be described as

$$u_{DS} \approx R_{DS(on)} i \tag{2.30}$$

where $R_{DS(on)}$ is the MOSFET on-state resistance. If the current instead flows through a body diode, the voltage drop is approximately equal to the diode forward voltage U_F [12]. These effects reduce the effective voltage applied to the machine and introduce uncertainty in the phase voltage. This is most noticeable at low speed, where the commanded voltage is small and the dead time becomes relatively large compared to the duty cycle.

2.3 Control system

The control system is responsible for operating the electric drive system such that the PMSM produces the desired mechanical behaviour. Depending on the application, the desired reference can be position, speed or torque. The controller uses measurements or estimations of the drive system state and calculates the voltage references that should be applied by the inverter to achieve the requested operating point.

In this project, the control system is implemented in a Microcontroller Unit (MCU). The MCU has access to measurements of the DC-link voltage, the stator phase currents and the rotor angle from the encoder. These signals are needed to synchronize the control with the rotor position and to determine how the inverter should be switched. The output from the controller is a set of PWM signals to the inverter gate drivers, which control the MOSFETs and thereby the voltages applied to the stator phases.

The control system is built as a cascaded control structure, meaning that there is a chain of regulators, commonly Proportional-Integral (PI), where each regulator provide the reference to the next regulator. In this structure, it is essential that the inner loops exhibit significantly faster dynamics than the outer loops. This ensures that the inner loops can track their reference values before the outer loop updates them, allowing the corresponding physical quantities time to respond.

In Figure 2.6 a block diagram of the cascaded control structure is shown, where the outermost regulator is a speed regulator. The speed regulator calculates a torque

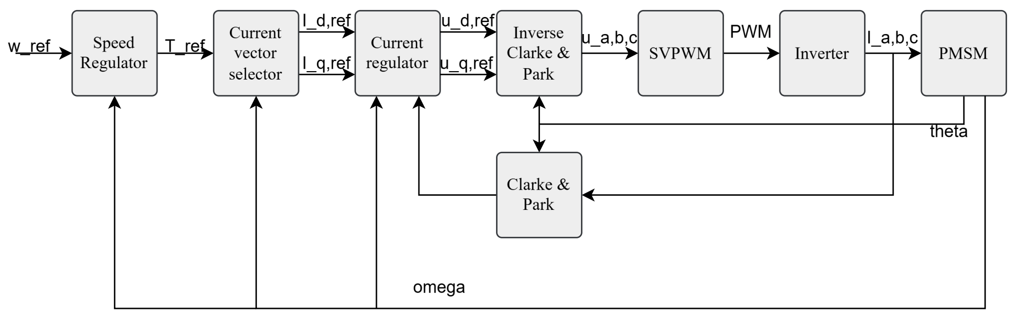

Figure 2.6: Cascade control structure for the electric drive system.

reference based on the speed error, the torque reference is converted into d- and q-axis current references for the current controllers. The current controllers calculate what d- and q-axis voltage is needed to reach the references based on the measured phase currents that have been transformed to the dq-system. Additionally the current controller has access to the rotor speed such that the induced voltage caused by the rotating magnetic fields can be compensated for.

A central part of the control system is the selection of the current vector reference. Since the torque of a salient-pole PMSM, shown in (2.22), depends on both the permanent magnet torque and the reluctance torque, there are several possible combinations of i_d and i_q that produce the same torque. The selected current vector affects the current magnitude, voltage requirement, losses and available speed range. Depending on the current operating point of the machine, there are different approaches to choosing the current vector, in the following sections some methods for current vector selection are explained.

2.3.1 MTPA

Maximum Torque Per Ampere (MTPA) is a control strategy used to minimize the current magnitude for a given torque demand, thereby reducing the resistive losses and improving efficiency. For a salient-pole PMSM, the torque expression includes both torque from the permanent magnets and reluctance torque. By properly selecting the current components i_d and i_q, it is possible to exploit the reluctance torque and reduce the required current magnitude.

For a given torque level, the possible combinations of i_d and i_q current components can be found by rearranging (2.22) such that i_q is expressed in terms of i_d and the torque T_e.

$$i_q(i_d, T_e) = \frac{T_e}{p(\Psi_m + (L_d - L_q)i_d)}. \tag{2.31}$$

This equation will result in a constant torque curve in the dq-plane where any combination of i_d and i_q will result in the same torque. Finding the point on this curve that is closest to the origin will thus be the MTPA point for that given torque.

The MTPA angle points can be derived analytically from the linear model equations by differentiating the torque equation, (2.22), with regard to the current vector angle in the dq-frame. Using the current magnitude and angle, the torque equation can be written as,

$$T_e(I_{dq}, \beta) = p(\Psi_m I_{dq} \sin(\beta) + (L_d - L_q)I_{dq}^2 \cos(\beta)\sin(\beta)) \tag{2.32}$$

where $I_{dq} = \sqrt{i_d^2 + i_q^2}$ is the current magnitude in the dq-frame and $\beta = \tan^{-1}(\frac{i_q}{i_d})$ is the current vector angle from the positive d-axis. To find the optimal current angle that maximizes the torque for a given current magnitude, the following equation has to be solved,

$$\frac{\partial T_e(I_{dq}, \beta)}{\partial \beta} = 0. \tag{2.33}$$

Using the trigonometric identity, $2\cos(x)\sin(x) = \sin(2x)$, the derivative of the torque with regard to the current angle is

$$\frac{\partial T_e(I_{dq}, \beta)}{\partial \beta} = p(\Psi_m I_{dq} \cos(\beta) + (L_d - L_q)I_{dq}^2 \cos(2\beta)). \tag{2.34}$$

Now solving (2.33) for β using the trigonometric identity, $\cos(2\beta) = 2\cos^2(\beta) - 1$, gives,

$$\beta_{MTPA}(I_{dq}) = \pm \cos^{-1}\left(\frac{-\Psi_m + \sqrt{\Psi_m^2 + 8(L_d - L_q)^2 I_{dq}^2}}{4(L_d - L_q)I_{dq}}\right) \tag{2.35}$$

where the positive angle results in a positive torque and the negative angle in a negative torque.

This results in a non-linear relationship between i_d and i_q, appearing as a curve in the dq-frame. To reduce the complexity of the calculations that are necessary to calculate the current references at each control loop update, the MTPA trajectory is often approximated using a linear relationship between the d- and q-axis current component references, such as,

$$i_{d,ref} = k_{MTPA} i_{q,ref} \tag{2.36}$$

where,

$$k_{MTPA} = \frac{1}{\tan(\beta_{MTPA}(I_{dq,max}))} \tag{2.37}$$

where k_{MTPA} is a linear constant and $I_{dq,max}$ is the maximum current that the drive system can sustain.

2.3.2 Field weakening

Field weakening is used when the machine reaches a speed where the inverter can no longer supply the voltage magnitude needed to reach the requested current reference. As the speed increases the voltage caused by the back-EMF gets larger, eventually all voltage supplied by the inverter is needed to counteract the back-EMF. At this point no current will be able to flow through the windings, and no torque will be produced, stopping the machine from accelerating further.

To be able to reach higher speeds, or higher torque at a given voltage magnitude, the back-EMF has to be reduced. This can be done by reducing the effective d-axis flux linkage, Ψ_d, that is inducing a voltage in the q-axis voltage equation, (2.18). By adding a negative i_d current, Ψ_d will be reduced according to (2.15), allowing more of the voltage supplied by the inverter to be used to drive a torque producing current.

However, field weakening comes at a cost of increased current magnitude and thereby increased resistive losses. Additionally, if the machine is operating at its current limit, producing its max torque according to MTPA, the field weakening is impossible without losing torque. This is because the decrease in i_d would have to come at a cost of i_q magnitude to stay below the current limit, thus changing the current angle and moving away from the MTPA angle.

2.3.3 MTPV

Maximum Torque Per Volt (MTPV) is a control strategy used in high speed operation, where the inverter voltage is the dominant constraint and an increase in negative i_d no longer causes a decrease in the required voltage magnitude. While MTPA maximizes the torque for a given current magnitude, MTPV maximizes the torque under the voltage limit described in (2.27).

Using (2.19) and (2.20), the voltage limit can be written in terms of the linear voltage equations in steady-state as,

$$(R_s i_d - \omega L_q i_q)^2 + (R_s i_q + \omega(L_d i_d + \Psi_m))^2 \leq U_{dq,max}^2. \tag{2.38}$$

This equation shows that the required voltage depends on both the resistance and the speed-dependant terms. Because of the term $L_d i_d + \Psi_m$, there is a point where negative i_d will cause it to swap sign such that increasing the negative i_d even more will result in higher voltage drop instead of reducing it. The resistance terms result in a voltage drop with the current magnitude, meaning that the resistive voltage drop is minimized by minimizing the current magnitude.

For high speed operation, the voltage drop over the resistance is often neglected, reducing the voltage limit to,

$$(L_q i_q)^2 + (L_d i_d + \Psi_m)^2 \leq \left(\frac{U_{dq,max}}{\omega}\right)^2. \tag{2.39}$$

The inequality constraint describes a set of current vectors, forming ellipses in the dq-plane, that are realizable given the speed and voltage limit. In the case where the resistance is neglected, these ellipses are centred on,

$$(i_d, i_q) = (-\frac{\Psi_m}{L_d}, 0) \tag{2.40}$$

and the size of the ellipses increases with increased $U_{dq,max}$ and decreased speed. However if the voltage drop over the resistance relative to available voltage is large, either due to high stator resistance or low DC-link voltage, then the ellipses will be shifted and rotated. This results in the MTPV trajectory including the resistance not being constant in the dq-plane.

The MTPV trajectory is found by maximizing the torque produced along the voltage ellipses. Physically, this means finding the current direction where the available voltage is used most effectively for torque production. In this work, the MTPV points are calculated numerically to avoid overly complex analytical expressions or simplifications like neglecting the stator resistance. This is done by finding the constant torque curve described by (2.31) with highest torque that tangents the voltage ellipse for the voltage limit and current speed, the intersection between theses lines will be the MTPV point.

2.4 Theoretical current and voltage limits for the salient-pole PMSM

The electric drive system used in this project can be modelled using the theory presented in previous sections. The linear model parameters that are used in theoretical analysis of the salient-pole PMSM that is evaluated in this project are found in Table 2.1, together with the voltage and current limits of the complete drive system. The current is limited by inverter components, such as MOSFETs and shunt resistors,

Table 2.1: Linear PMSM model parameters and drive-system limits.

Parameter	Symbol	Value
Pole pairs	p	2
Stator resistance	R_s	0.026573 Ω
d-axis inductance	L_d	0.115 mH
q-axis inductance	L_q	0.210 mH
Permanent magnet flux linkage	Ψ_m	0.008717 Wb
DC-link voltage	U_{dc}	12 V
Maximum current magnitude	$I_{dq,\max}$	70 A

where higher currents could cause damage. The power supply used in the project outputs a DC voltage of 12 V, which corresponds to $U_{dq,max} = 8.49$ V according to (2.26).

In Fig 2.7, the current and voltage limits are plotted in the dq-plane for d- and q-axis currents of ±100 A. The current limit for the drive system is shown as a circle around the origin with the radius equal to $I_{dq,max}$. Constant torque curves are drawn according to (2.31), showing what combination of i_d and i_q currents result in a given torque level. The maximum torque within the current limit of 70 A is 1.46 Nm according to the linear model. The MTPA trajectory of the machine is plotted with the current angle calculated using (2.35) for each current amplitude, for both motor and generator operation. At the current limit, the MTPA angle is 26.86° from the q-axis.

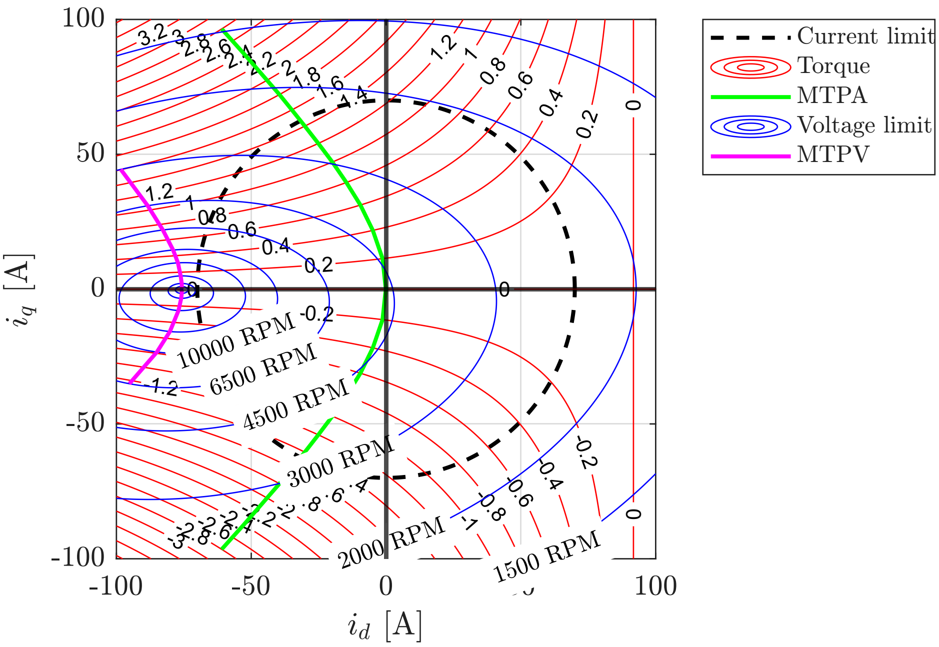

Figure 2.7: Theoretical constant torque curves, voltage ellipses, MTPA and MTPV trajectories, in the dq-plane, for the electric drive system.

The voltage limit ellipses are plotted according to (2.38), for constant $U_{dq,max} = 8.49$

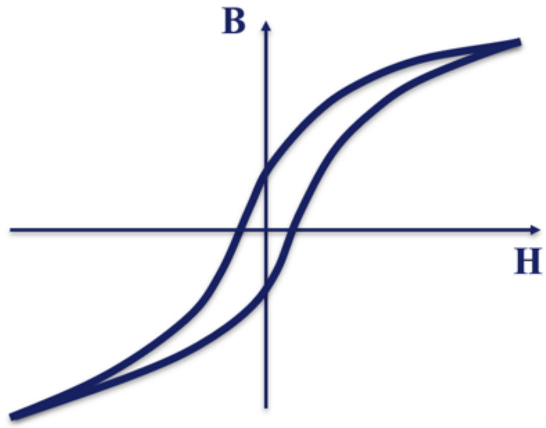

Figure 2.8: General B-H curve showing magnetic saturation and hysteresis.

V and increasing speeds. Voltage ellipses for 1500 RPM up to 10000 RPM have labels, ellipses for higher speeds continue to decrease in size. As the speed goes toward infinity, the ellipses centre closes in on the point described by (2.40). For this specific machine, this point is located at $i_d = 75.8$ A, and thereby outside of the current limit of the drive system. As can be seen in the figure, the theoretical MTPV trajectory is also outside of the current limit.

The base speed of the machine refers to the speed where the corresponding voltage ellipse intersects the MTPA point at the current limit. At higher speeds than base speed, the maximum torque that can be produced is no longer along the MTPA trajectory. Instead field-weakening is required to reach the maximum torque available at that speed which will be lower than at MTPA. For this machine the theoretical base speed is 2381 RPM.

2.5 Non-linear effects and losses

The linear PMSM model is useful for describing the main relationship between current, voltage, flux linkage and torque. However, in practice there are multiple effects and losses that can cause the behaviour of an electric machine to deviate from the linear model and lose efficiency. When operating the electric machine at a wide range of currents, speeds and temperatures, these deviations can become more or less substantial.

2.5.1 Magnetic saturation

In the linear model magnetic flux density is assumed to increase linearly with magnetic field strength, according to (2.2). This relation is only valid in the approximately linear region of the magnetic material. In practice, the iron in the stator and rotor follows a non-linear B-H curve, like the one shown in Figure 2.8. At higher flux densities, the material reaches saturation when a further increase in field strength no longer leads to the same increase in flux density. Since the inductances in the linear model corresponds to how much flux linkage is produced for a given current, saturation causes the effective inductance to change with the operating point.

2.5.2 Cross inductance

When multiple magnetic loops are in proximity to each other, the magnetic flux from one loop can link with another loop. This happens when the magnetic flux density produced by a current in one winding links with another winding. This can be written as [8],

$$\Psi_{12} = L_{12} I_1 \tag{2.41}$$

where Ψ_{12} is the flux linkage in winding 2 caused by the current, I_1, in winding 1 and L_{12} is the cross inductance from winding 1 to winding 2. For a PMSM this could be written as,

$$\Psi_d = L_d i_d + L_{qd} i_q + \Psi_m \tag{2.42}$$

$$\Psi_q = L_q i_q + L_{dq} i_d. \tag{2.43}$$

Combining the effect of both magnetic saturation and cross inductance, the flux linkages can generally be described as,

$$\Psi_d = \Psi_d(i_d, i_q) \tag{2.44}$$

$$\Psi_q = \Psi_q(i_d, i_q). \tag{2.45}$$

2.5.3 Temperature dependence

Temperature variations affect several machine parameters. The stator resistance increases linearly with temperature according to [13],

$$R = R_0(1 + \alpha_{cu}(T - T_0)) \tag{2.46}$$

where $\alpha_{cu} = 0.393\,\%/°\mathrm{C}$ is the temperature coefficient of electrical conductivity for copper. The permanent magnet flux linkage Ψ_m decreases with temperature as the NdFeB-magnets weaken. For this type of magnets, the weakening is typically about $0.11\,\%/°\mathrm{C}$ [14]. Within reasonable temperatures, the weakening of the permanent magnets is reversible.

2.5.4 Iron losses

Iron-losses, also referred to as core losses, occur in the magnetic material in the machine due to time varying magnetic fields. These losses mainly consists of hysteresis and eddy currents. Hysteresis is caused by the change in flux density lagging behind the change in field strength. In Figure 2.8, the hysteresis effects creates the closed loop in the B-H curve. When the field strength is increased from zero, a corresponding flux density will be created, but when the field strength is reduced again to zero, there will be permanent magnetization left in the material. To remove the magnetization a negative field strength has to be applied. The area of the loop in the B-H curve is the energy loss over each electric period per unit volume [9].

Voltage is induced by a time-varying magnetic flux in a winding according to Faraday's law, (2.7). However it is not only in the windings that this can happen, but also in the iron core itself. Since the iron core has a certain resistivity, the induced voltage give rise to so-called eddy currents.

Iron losses can be modelled using the Bertotti iron loss equation. It expresses the combined iron loss from hysteresis, eddy currents and excess loss as [15],

$$P_{Fe} = k_h B_m^2 f + k_d B_m^2 f^2 + k_e B_m^{1.5} f^{1.5} \tag{2.47}$$

where k_h, k_d, k_e are coefficients specific to the used material and shape relating to hysteresis, eddy currents and excess loss components respectively. Additionally f is the frequency of the magnetic field and B_m is the maximum magnetic flux. As can be seen, the iron losses has a strong dependence on the frequency and thereby the rotational speed of a electrical machine.

2.5.5 Copper losses

Copper losses arise from the resistance in the copper wire in the windings. This resistance causes a voltage drop, which is an important part of the linear model. The power loss caused by the resistance is given by,

$$P_{Cu} = \frac{3}{2K^2} R_s (i_d^2 + i_q^2). \tag{2.48}$$

This power loss results in heat radiated from the stator windings and is proportional to the square of the current magnitude.

3

Method for experimental mappings

This chapter describes the methods used to experimentally measure the characteristics of the salient-pole PMSM in the electric drive system described in Section 2. The salient-pole PMSM is referred to as the test machine here to distinguish from the load machine that is used as mechanical load. In the following sections, the test bench setup used for measurements and the automation of measurements are described.

3.1 Equipment overview

The test bench used to perform measurements on the test machine is shown in Figure 3.1. It consists of the test machine, a load machine and an inline torque sensor connecting the shafts of the test and load machine. The shafts are connected using bellows couplings that have high torsional stiffness but can compensate for slight misalignment of the shafts, vibrations or thermal expansion. The test machine is connected to the circuit board that houses the inverter and the MCU used to control the machine. Not shown in the figure is the DC power supply that provides the 12 V DC-link to the inverter and controller.

Additionally, the machine was equipped with an encoder directly on the output shaft and a temperature sensor in the stator windings, both of which were connected to the MCU. The encoder used was an incremental encoder, meaning that it cannot determine the absolute rotational angle of the shaft. Instead it senses changes in angle and increments the angle by counting how many slots on a disc that rotates with the shaft that passes a sensor that is fixed. The encoder used has a resolution of 4096 increments per mechanical rotation. The temperature sensor was a thermistor which has a temperature dependant resistance that is known. The MCU senses the voltage drop over the thermistor and can calculate the resistance and thereby the temperature.

The MCU also has analogue inputs for measurements of the phase currents and the DC-link voltage. Having the measurement of the DC-link voltage allows the voltage to vary slightly from the ideal set point, while still being able to calculate the duty

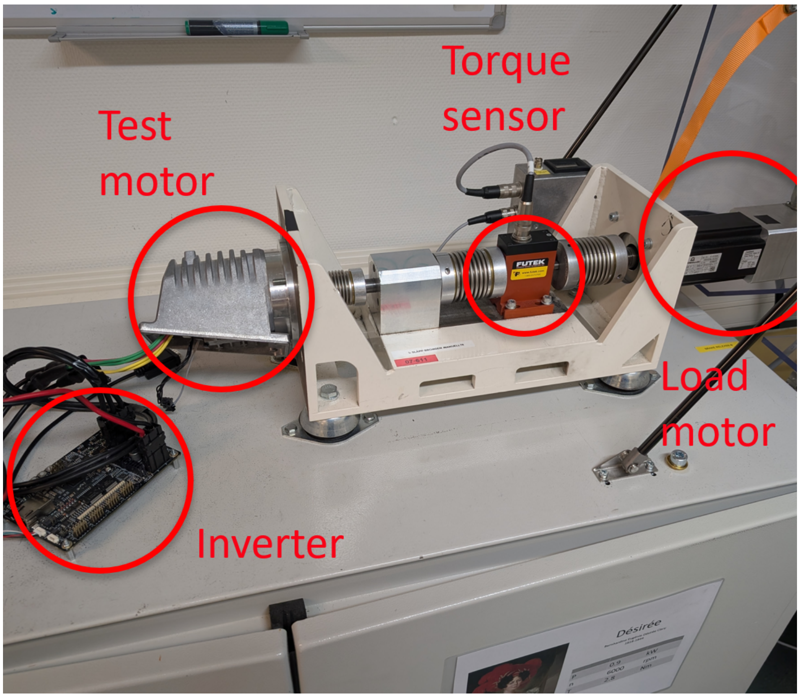

Figure 3.1: Overview of the test bench setup.

cycles for the inverter accurately. The MCU estimated the average phase voltages based on the DC-link voltage and the duty cycles that were given to the inverter. However, this estimation does not consider voltage drops over the transistors described by (2.30), diode voltage drop, nor does it compensate for the dead time described by (2.29).

A Baumüller three-phase PMSM was used as load machine during the measurements. This machine has a similar drive system to the one described for the test machine. It is rated for 2.8 Nm of torque and a maximum rotational speed of 6000 RPM. The load machine was speed regulated while the test machine was producing varying torques to the joint shaft, hence the speed regulator of the load machine had to compensate with a counteracting torque. Since the available torque from the load machine is higher than the highest obtainable torque from the test machine, given the current limits, the test machine cannot overpower the load machine and cause uncontrollable acceleration.

Communication with the controllers for the test and load machines, as well as with the Analogue to Digital Converter (ADC) for the torque sensor, was handled over a Controller Area Network (CAN) bus. In this way, a separate computer can both read from or write to specific memory addresses on the devices where references for regulators or measurements are stored.

3.1.1 Torque sensor configuration

The torque sensor mounted between the two machines determined the torque by measuring a small twist in the shaft. The sensor output a voltage that was converted to a digital signal using an ADC. The ADC sampled the analogue signal and applied a moving average to reduce noise in the torque signal. The moving average in the ADC module could be configured using a couple of parameters. Firstly, the number of samples included in the averaging window could be adjusted. This was done through two parameters, the number of accumulated samples n and the window size m following,

$$x_{accu} = x_{(1)} + x_{(2)} + ... + x_{(n)} \tag{3.1}$$

$$x_{avg} = \frac{x_{accu(1)} + x_{accu(2)} + ... + x_{accu(m)}}{n \cdot m}. \tag{3.2}$$

where $x_{(n)}$ is a sampled torque value, $x_{accu(m)}$ is the sum of the accumulated samples and x_{avg} is the average of all samples collected in the average window. Additionally, the sampling frequency was adjustable between 1 Hz and 15 kHz. Together, the number of samples and the sampling frequency determined the time period over which the average was performed. A long time period resulted in slow filtering that lagged the real torque value. However, an excessively short time window caused low frequency noise to remain as its period was longer than the averaging time window.

In this work, an accumulated number of samples $n = 128$, window size $m = 32$ and a sampling frequency of 10 kHz were chosen, providing a balance between decently fast response and effective noise suppression. With this configuration a minimum of 0.4 seconds was required to replace all samples in the window for the moving average.

3.2 Measurement script

To achieve consistent measurements and facilitate the process of acquiring a complete dataset capturing the machine characteristics, an automated mapping script was developed. The script was written in Python and used libraries developed by Aros Electronics AB to communicate with the test machine, the load machine and the torque sensor over CAN. Figure 3.2 shows a diagram of the communication structure between the test machine, load machine, torque sensor and the script.

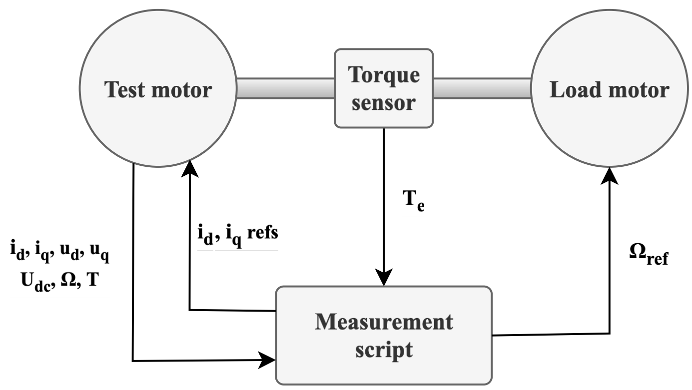

Figure 3.2: Block diagram of signal communications.

The developed measurement script uses Python's threading library to enable concurrent execution of the polling loop, which continuously acquires new measurements, and the mapping logic loop, which sets references and processes the incoming data. Although this is not true CPU-level parallelism because Python threads are still constrained by the Global Interpreter Lock (GIL), it is still effective since the polling and control tasks are largely Input/Output-bound and benefit from overlapping execution [16].

For each loop in the polling thread, the script requests measurements from the test machine and the torque sensor over CAN. From the torque sensor, the torque value that have been processed by the ADC, according to Section 3.1.1, is received. From the test machine, the currents and voltages in the dq-frame, together with the DC-link voltage, mechanical speed and stator temperature is received. Each measurement is requested sequentially in the loop, causing the measurements to be slightly shifted in time, limiting the usage of the script to steady-state measurements since the transients can not be accurately captured. The polling loop was limited to run at 50 Hz to get consistent timing between each sample. This was slightly below the maximum achieved frequency for the polling loop, meaning that all the measurements where collected in less than 0.02 seconds. The measurements from each loop is stored in a dictionary that is sent to a queue that the mapping logic thread can access. Each dictionary of measurements is referred to as a sample.

The mapping logic loop controls the overall execution of the measurement sequence, deciding when different references should be sent to the test and load machines. In Figure 3.3, a flow chart of the mapping logic loop is presented. Before the main loop is started, communication is initialized with all devices, initial references are set to safe values and the absolute encoder angle is determined. This is done by a rotor alignment procedure that defines the electrical zero position for the incremental encoder. The rotor alignment is done by applying a current through phase a of the machine, while the shaft is unloaded, causing the permanent magnetic field from the rotor to align with the induced field. This causes phase a, the α-axis and the d-axis to be aligned and defines the rotor position as $\theta = 0$.

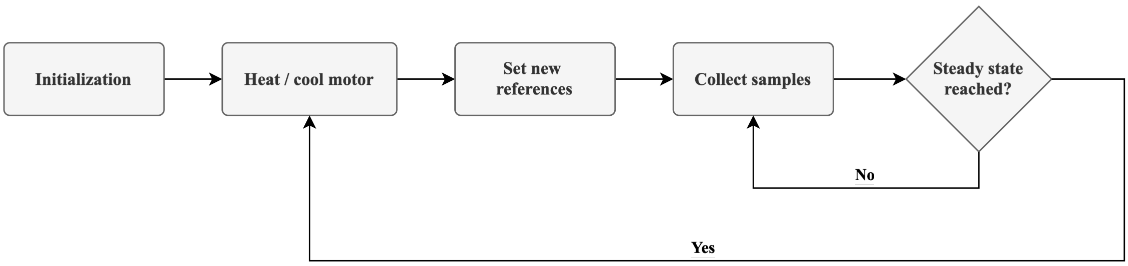

Figure 3.3: Block diagram of mapping sequence logic loop.

After the initialization, the mapping logic loop iterates through a predefined sequence of operating points defined in Section 3.2.1. For each operating point, the loop starts by ensuring that the test machine is within the temperature range. The operating points are ordered such that lower temperatures are executed first, each time the temperature reference increases the heating procedure defined in Section 3.2.2 is performed until thermal equilibrium is reached. If the temperature deviates more than $\pm 5\,°C$, between operating points with the same temperature reference, then either heating is performed using the method in Section 3.2.2 or cooling is done passively by setting the currents to zero.

When the temperature reference is met, the speed reference is set on the load machine and the current references are set on the test machine. The mapping loop then collects samples of measurements from the polling loop to check if the system has reached steady state. The method used to check if steady state had been reached is defined in Section 3.2.3. The mapping loop need to collect 15 samples in a row that fulfill the steady state conditions in order to be able to move on to the next operating point. The samples of measurements collected in steady state for each operating point are averaged and then saved together with the references to be used for the analysis.

3.2.1 Operating points for mapping sequence

The mapping logic loop takes a sequence of operating points as input that is iterated over to collect measurements at each operating point. An operating point is defined as the set of references for speed, Ω, d-axis current, i_d, q-axis current, i_q, and the stator temperature, T_s. This sequence determines what part of the dq-plane is evaluated during the mapping by the range of the current references. The set of current references is then evaluated for different speeds and temperatures.

The generation of current vector references were automated using a script that distributed the current operating points evenly within the given limitations. Limitations could be set using upper and lower bounds on the current vector components i_d and i_q, the current magnitude, $I_{dq} = \sqrt{i_d^2 + i_q^2}$, and the current angle, $\beta = \tan^{-1}(i_q/i_d)$. The evaluated operating points were chosen to get the widest possible range of current vector combinations given the constraints of the drive system. Because of the unidirectional power supply, the q-axis current was limited to $i_q \geq 0$ and the current limit of the drive system limits the current amplitude to $I_{dq} \leq 70$ A.

Based on the set limits, the current references were then generated by the script in a polar arrangement in the dq-plane. Specifically, the points are placed on circles centred at the origin, with increasing radius corresponding to the increasing current magnitude. This structure ensures coverage of the operating region, while aligning naturally with the interpretation of current magnitude and current angle. Additionally, it provides a convenient and uniform method to limit the maximum current magnitude in the dq-plane.

The resolution of the current reference distribution was controlled by two parameters, the radial step size and the arc spacing. The radial step size determines the increment in current magnitude between circle arcs, while the arc spacing determines the arc distance between two neighbouring points on the same circle arc. This was done instead of spacing points based on magnitude and angle to get similar spacing between points at different current magnitudes. These parameters are used to balance the measurement resolution to the required measurement time. For the mapping performed on the test machine in this project, the sequence of current references can be seen in Figure 3.4, where both the radial step and arc step was set to 5 A.

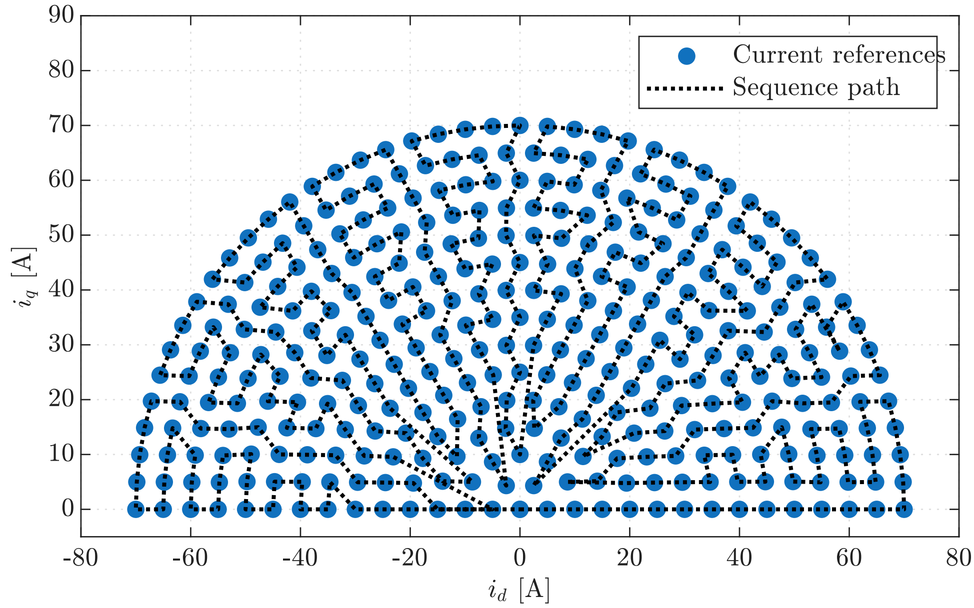

Figure 3.4: Sequence of current reference points in the *dq*-plane with segmentation.

Additionally, thermal effects are taken into consideration when generating the sequence of current references. Since high current magnitudes result in larger resistive losses, according to (2.48), where the energy is converted into heat, operation at high currents for a prolonged time requires excessive cooling. To reduce the cooling requirements, the current references where divided into circle segments. For each segment the sequence first sweeps references toward the maximum amplitude, then zigzags between the remaining references in the segment toward smaller and smaller amplitudes. In Figure 3.5 the effect of the segmentation for the accumulated energy from resistive losses over time is shown. Clearly the same total energy is achieved after the complete sequence, but using segmentation the average heating power is more consistent over the time.

To capture possible speed and temperature dependencies of the machine, the selected sequence of current vectors where tested for the speeds of 500, 1000, 1500 and 2000 RPM and temperatures of 50 °C, 70 °C and 90 °C. The maximum speed tested was 2000 RPM since the voltage limit for higher speeds would cause some points within the current limit to not be obtainable. Higher speeds would also require a power supply that could handle larger currents on the DC-link since the power draw increases but the voltage is kept constant at 12 V. With the sequence of current vector references shown in Figure 3.4, having 346 combinations of i_d and i_q, together with the 12 combinations of speed and temperature references, a total of 4152 operating points were evaluated.

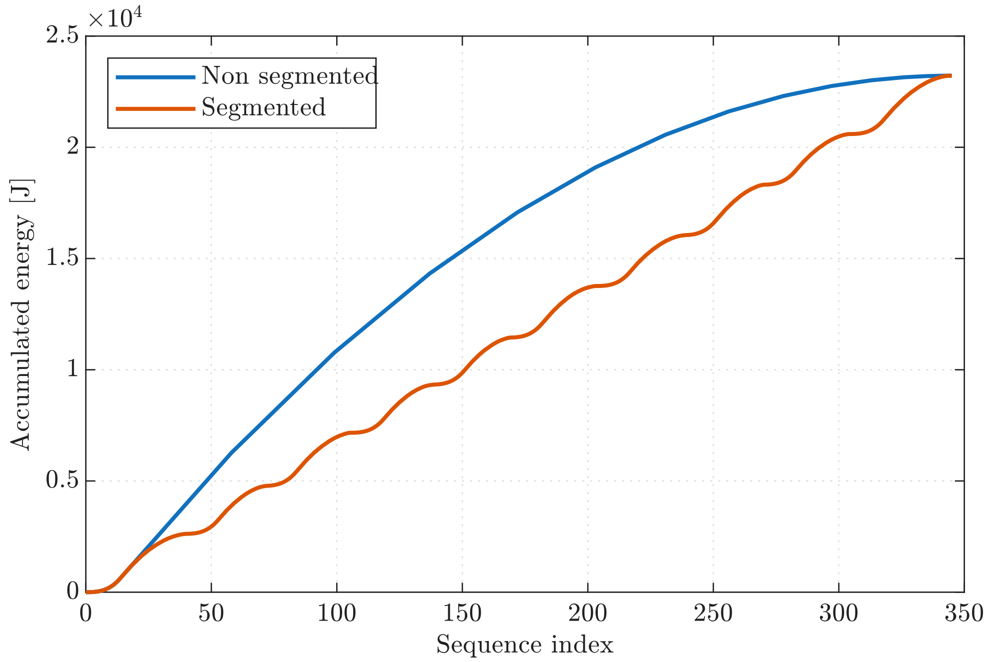

Figure 3.5: Accumulated energy in the machine over the sequence.

3.2.2 Stator temperature control

To heat the test machine to the temperature specified for the operating point that is evaluated, a controlled d-axis current is used, causing resistive losses in the stator to heat the machine. To allow the machine to heat evenly, not just the stator windings but also the iron core, housing and rotor, a PI controller was used. This regulates the current such that the stator temperature, T_s, reaches the reference, $T_{s,ref}$, then keeps it constant to allow the heat to radiate to the rest of the machine until a thermal steady state is reached. This thermal steady state was found when the heating current, controlled by the PI controller, had been kept constant for 30 minutes.

The PI controller was implemented using the following equations,

$$e = (T_{s,ref} - T_s) \tag{3.3}$$

$$i_d = k_p e + k_i \int (e)dt \tag{3.4}$$

where e is the temperature error, and k_p, k_i are tunable gain parameters. For the lab equipment used, the gains $k_p = 2$ and $k_i = 0.05$ were chosen. Additionally, the maximum heating current magnitude was limited to 90 % of the maximum current amplitude of the machine. The integrator contribution was limited to 80 % of the maximum allowed heating current, to limit integrator wind-up.

3.2.3 Steady state detection

Since the goal of the measurement script is to find the steady state characteristics of the machine, the script needs to both detect when steady state is reached and when enough samples have been collected for each operating point. A sample is considered to be steady state when the speed and currents have been within predefined tolerance bands from their respective reference for W samples. Additionally, the torque derivative needs to have stabilized over the last W samples. W is a design variable for the window length used in the steady state detection algorithm and was set to 10 samples.

The condition for the currents, i_d and i_q, and speed, Ω, to reach steady state for sample k is:

$$|i_{d,avg}(n) - i_{d,ref}(k)| < i_{d,tol}, \qquad \forall n \in \{k - W + 1, \dots, k\} \tag{3.5}$$
$$|i_{q,avg}(n) - i_{q,ref}(k)| < i_{q,tol}, \qquad \forall n \in \{k - W + 1, \dots, k\} \tag{3.6}$$
$$|\Omega(n) - \Omega_{ref}(k)| < \Omega_{tol}, \qquad \forall n \in \{k - W + 1, \dots, k\} \tag{3.7}$$

where $i_{d,ref}$, $i_{q,ref}$, Ω_{ref} are the references for the specific operating point. The average currents $i_{d,avg}$ and $i_{q,avg}$ are filtered to remove harmonics.

The steady state condition for the torque is defined by the following condition,

$$\left| \frac{\text{med}(T_{\text{last}}) - \text{med}(T_{\text{first}})}{\text{med}(t_{\text{last}}) - \text{med}(t_{\text{first}})} \right| \leq \dot{T}_{\text{tol}} \tag{3.8}$$

where med is the median operator, $\dot{T}_{\text{tol}}$ is the maximum allowed change in torque in Nm/s and,

$$T_{\text{first}} = \{\, T(k) \mid k = t - W + 1, \dots, t - W/2 \,\}, \tag{3.9}$$
$$T_{\text{last}} = \{\, T(k) \mid k = t - W/2 + 1, \dots, t \,\}. \tag{3.10}$$

This approach is adopted since there is no torque reference value during the mapping procedure, yet the torque needs to have reached its steady state value. The median based method is used instead of a linear regression over the window to reduce the effect of outliers in the torque measurements. This approach was adopted before averaging was performed on the ADC for the torque sensor measurements, which effectively removes outliers before they reach the measurement script, but worked well for the task regardless.

3.3 Measurement of R_s and Ψ_m

Having accurate estimations of R_s is important to be able to calculate the flux linkages, Ψ_d and Ψ_q using (2.18) and (2.17) in steady state, from the measurement data for each operating point. These flux linkages are in turn used to calculate inductances from (2.42) and (2.43) as well as being an important part of the flux based model for simulation. Although Ψ_m is not used explicitly in calculations or for the flux based model, it was measured to get an understanding of what impact it has on Ψ_d. For this project R_s and Ψ_m are modelled as only being dependant on temperature, hence they where measured for 50 °C to 90 °C with 10 °C increments.

While heating the machine using the method described in Section 3.2.2, R_s and Ψ_m were measured periodically with 60 second intervals. Measurements were taken until the measured Ψ_m had converged for the specific stator temperature, indicating that also the rotor had reached a steady state temperature. After Ψ_m had converged, at least 15 measurements of both R_s and Ψ_m were taken to get an average over, to mitigate noisy measurements.

R_s was measured by having the rotor stationary and driving a d-axis current and measuring the corresponding voltage needed. Since there is no rotating flux linkage and $i_q = 0$, R_s is calculated from (2.19) as,

$$R_s = \frac{u_d}{i_d}. \tag{3.11}$$

The permanent magnet flux linkage, Ψ_m is measured by rotating the test machine rotor using the load machine, generating a back-EMF that is measured. This is done by regulating the stator currents to zero and measuring what voltage that the inverter has to switch out to achieve this. Since there are no stator currents, there is no voltage drop from resistance or induced fields, and Ψ_m is calculated from (2.20) as,

$$\Psi_m = \frac{u_q}{\omega}. \tag{3.12}$$

4

Development of data driven PMSM model and current vector selector

4.1 Flux based machine model from mapped data

Based on the mapped machine data collected from the measurements described in the previous chapter, a Look-Up table (LUT) based machine model for use in Simulink was developed. In this way, possible non-linear effects like magnetic saturation and cross inductance can be captured. For this machine model the mapping performed at 2000 RPM and 50 °C was used to create the LUTs, hence possible dependencies on speed and temperature is not included in the model.

The model is based on the flux-based voltage equations (2.17) and (2.18), and utilizes LUTs that map the relationship between the flux linkages, Ψ_d and Ψ_q, and the stator currents, i_d and i_q as,

$$i_d = \mathrm{LUT}_{i_d}(\Psi_d, \Psi_q) \tag{4.1}$$
$$i_q = \mathrm{LUT}_{i_q}(\Psi_d, \Psi_q). \tag{4.2}$$

Additionally, another LUT is used to map torque from the currents as,

$$T_e = \mathrm{LUT}_{T_e}(i_d, i_q), \tag{4.3}$$

replacing the torque equation (2.22). To obtain the flux LUTs, the flux linkages Ψ_d and Ψ_q were calculated for each measured operating point of the machine, according to,

$$\Psi_d = \frac{u_q - R_s i_q}{\omega_e} \tag{4.4}$$

$$\Psi_q = \frac{u_d - R_s i_d}{\omega_e}. \tag{4.5}$$

To extend the model to operating regions not covered by measurements, certain symmetry assumptions were introduced. The measured torque was compensated for the offset torque measured at $i_q = 0$. This offset was estimated as the mean torque for operating points along the d-axis, which corresponds to 0.088 Nm. This offset likely comes from losses in friction and iron losses and could be added to the model using a speed dependant torque loss. This allows the torque to be symmetrically mirrored in the d-axis, such that,

$$T_e(i_d, -i_q) = -T_e(i_d, i_q). \tag{4.6}$$

Also the calculated flux linkages where mirrored in the d-axis following,

$$\Psi_d(i_d, -i_q) = \Psi_d(i_d, i_q) \tag{4.7}$$
$$\Psi_q(i_d, -i_q) = -\Psi_q(i_d, i_q). \tag{4.8}$$

With these assumptions, coverage of the third and fourth quadrants is achieved, even if they were not experimentally mapped.

Due to the polar arrangement in the mapping sequence generation, the measured current vectors are distributed over a circular region in the current plane. As a result, the data points do not lie on a structured grid. However, for efficient implementation of the LUTs in simulation and control, it is beneficial to represent the data in a rectangular grid. To achieve this, the measured data was interpolated on to a rectangular grid using the RBFInterpolator function from Python's SciPy library with a cubic radial basis function kernel [17]. This method was also used for extrapolation to extend the mapped data outside of the measurement range such that the behaviour of the machine is predictable even slightly outside of the measurement range. For the LUTs used in the Simulink simulation, the measured data was extrapolated up to ±110 A for both i_d and i_q.

4.2 Data-driven method for current vector selection

A current reference selector based on LUTs allows the controller to have insights into predicted machine behaviour at different operating conditions, before applying any reference values. In a cascaded control structure, as discussed in Section 2.3, each control layer provides the references for their inner loop controllers. The current vector selector transforms the torque reference to current references. Traditionally this might be done using a set of linear equations, to find a point along MTPA, paired with a feedback regulator that provides an additional field weakening current based on the voltage utilization. The LUT based current vector selector evaluated in this project instead uses LUTs that are the inverse of the LUTs used for the machine model, described in Section 4.2.

Since the inverse of the torque LUT for the model (4.3) is ambiguous, meaning that there are multiple current vectors that provide the same torque according to (2.31), an algorithm was used to pick the appropriate vector. The choice of current vector depends on the current and voltage limitations. The current limitation is constant in the dq-plane regardless of operating point. However, the voltage limitation does vary with speed and is affected by non-linear effects like saturation and cross inductance. To check if a current vector is within the voltage limitation, specified by (2.27), LUTs for the flux linkage depending on the current vector were used to predict the voltage requirement for a given current combination. From the flux linkage, the voltage is calculated, using (2.17) and (2.18), for the measured speed of the machine.

The goal of the algorithm is to, given the torque reference, find the current vector that produces the requested torque and is within the limitations. If the torque reference is not achievable within the limitations, the current vector that produces the largest possible torque is given. If no voltage limit is restricting the choice of current vector, the MTPA point corresponding to the torque reference from the speed regulator is chosen. However, if the voltage limit causes the MTPA point for the requested torque to be unachievable, then the current vector producing the requested torque should be chosen such that the voltage utilization is maximized, and thereby minimizing the current magnitude. Due to other limitations on the voltage utilization in the control structure, the voltage limitation is set to 95% of the theoretical $U_{dq,max}$ using SVPWM.

4.3 Test cases for current vector selector in simulation

To evaluate if the LUT-based current vector selector manages to select the appropriate current reference, depending on the load torque and speed reference, a number of test cases were developed. The test cases were developed such that different limitations was in effect depending on the speed of the machine and what torque reference was given by the speed regulator. Four test cases are presented here.

The first test case evaluates the ability of the current vector selector to follow the MTPA trajectory for a speed under the base speed, where no field weakening is required. This was performed by setting the speed reference to 2000 RPM and ramping the load torque from 0 to 1.45 Nm. This intentionally above the maximum torque that was measured during the mapping such that the current limit is reached. The load ramp is performed after the speed reference is reached.

The second test case performs the same ramp in load torque but at a higher speed of 4000 RPM. This case should evaluate the ability to follow a voltage limit ellipse for a constant speed up to the point where it intersects with the current limit. Further this should demonstrate the increase in achievable torque by utilizing field weakening.

The third test case tests the ability to resist a constant load torque while ramping the speed reference. This is done with a 0.6 Nm constant load torque followed by a ramp in the speed reference from 0 RPM up to a speed that can not be reached given the load. This tests the ability to set references close to the voltage limit such that the voltage utilization is maximized as the need for field weakening increases.

The forth test evaluates the current reference trajectory that is followed when a large step in the speed reference is performed. With a constant load at 0.4 Nm, the speed reference is set from 0 to 6000 RPM in an instantaneous step. The instantaneous step causes a large speed error which the speed regulator will try to counteract by requesting the maximum torque as reference to the current vector selector. Under base speed this should cause the current reference to be set as the MTPA point at the current limit. When speed increases above base speed, the voltage limit will become active.

5

Results

5.1 Torque maps and MTPA trajectories

The steady-state behaviour of the salient-pole PMSM was characterized through systematic mappings of torque, flux-linkages and voltage constraints in the current plane. The mappings were performed at the rotational speeds of 500, 1000, 1500 and 2000 RPM, as well as the temperatures of 50, 70 and 90 °C.

The case of 1000 RPM and 50 °C is used as a baseline for the analysis. The resulting torque surface for the baseline case is presented in Figure 5.1, where the red dots represents the measured points that are used in the interpolation. As expected for a salient-pole machine, the torque production consist of both torque from the permanent magnets and a reluctance torque component. This is evident from the torque contours, which have an asymmetrical profile in the *dq*-plane, where the maximum torque for a given current magnitude is achieved at an angle $\beta > 90°$. The maximum achieved torque is approximately 1.3 Nm.

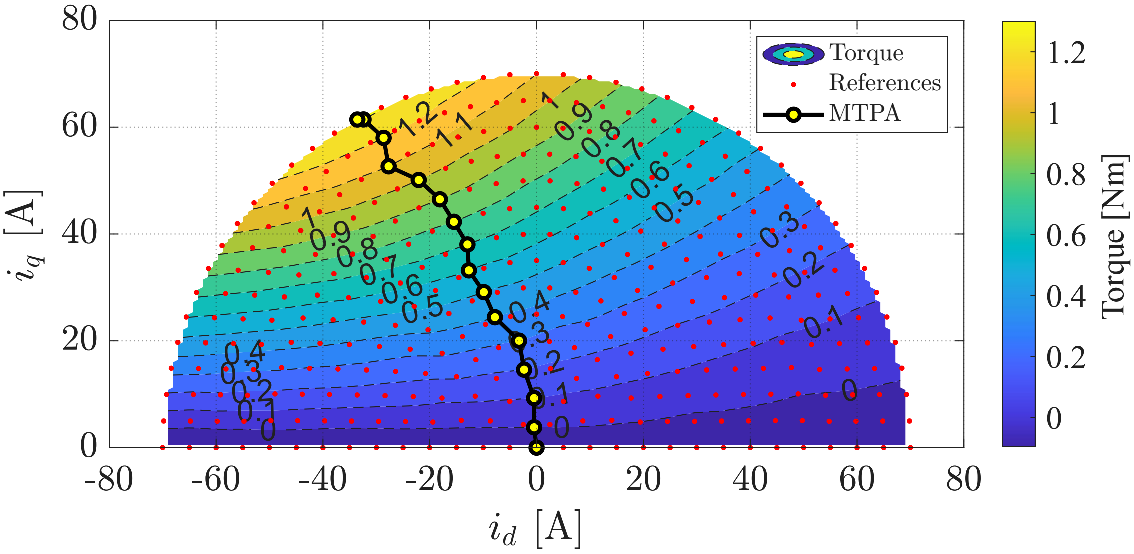

Figure 5.1: Torque map at 1000 RPM and 50 °C.

To investigate the speed dependency of the torque production, the point-wise difference between the torque maps at 500 RPM and 2000 RPM at 50 °C was calculated. The resulting torque difference map is presented in Figure 5.2.

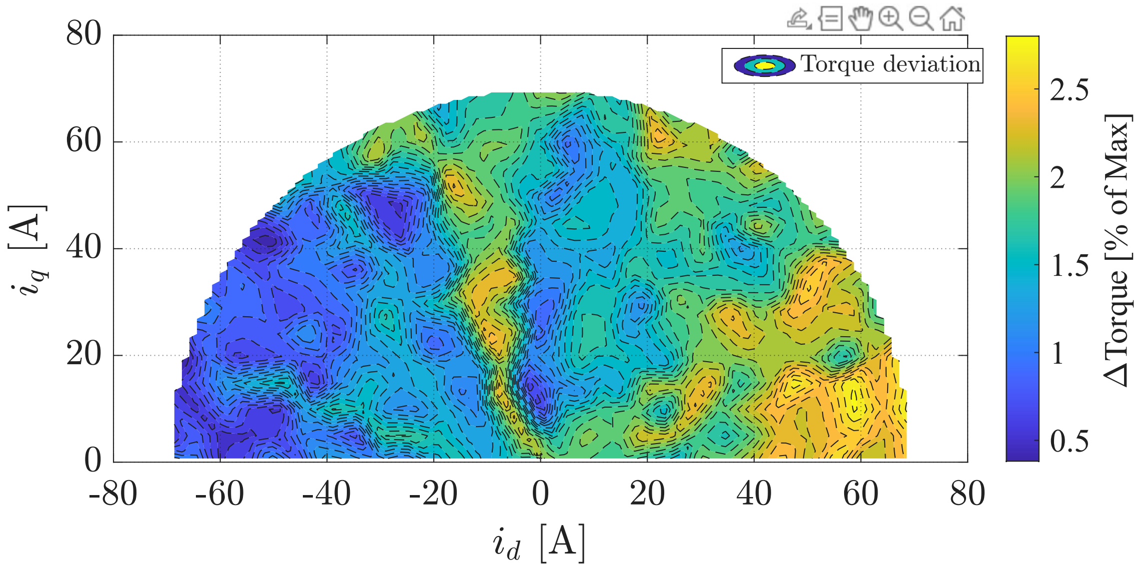

Figure 5.2: Torque deviation map between 500 RPM and 2000 RPM at 50 °C.

A systematic torque reduction can be observed across the entire current plane for higher speeds. The maximum torque deviation occurs in the right half plane and amounts to about 2.8 % of the maximum achieved torque at this temperature, which corresponds to approximately 0.036 Nm. In the field-weakening region in the left half plane, the difference in torque is significantly smaller.

Similarly, the impact of thermal variations was quantified by subtracting the torque map at 90 °C from the one at 50 °C at a rotational speed of 1000 RPM. The torque deviation map is presented in Figure 5.3.

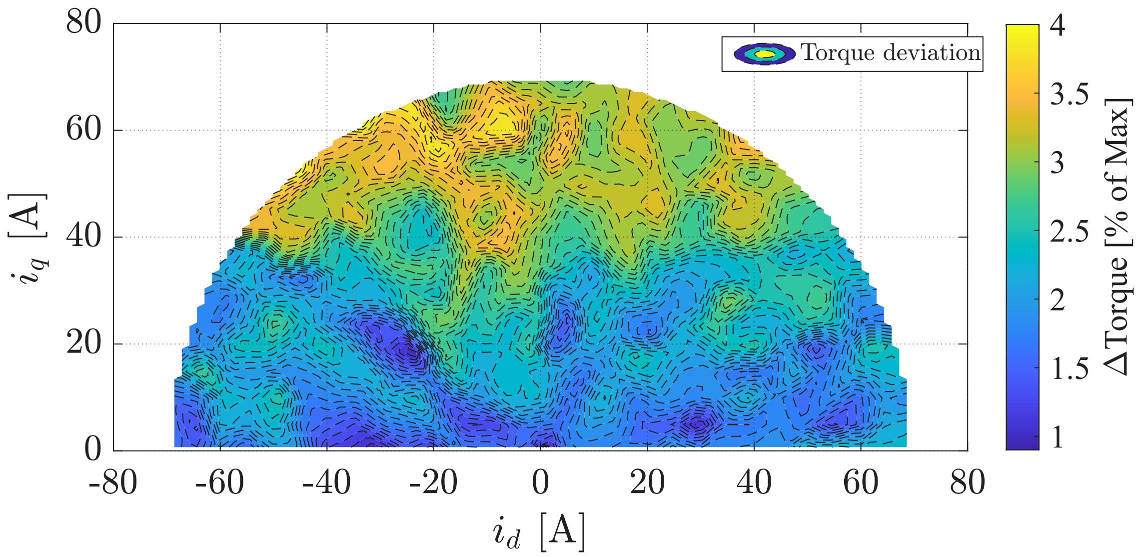

Figure 5.3: Torque deviation map between 50 °C and 90 °C at 1000 RPM.

Likewise to increasing speeds, increasing temperatures also show a systematic reduction in torque production across the entire current plane. The highest deviations in torque are present at high current magnitudes, particularly in the q-axis current. The maximum deviation amounts to 3.9 % of the maximum torque, which corresponds to around 0.05 Nm. For lower q-axis currents, where overall torque production is low, the difference is smaller but still present.

The MTPA trajectories were extracted from the torque surfaces at both the lowest and highest speeds and temperatures. These four MTPA trajectories are presented in Figure 5.4.

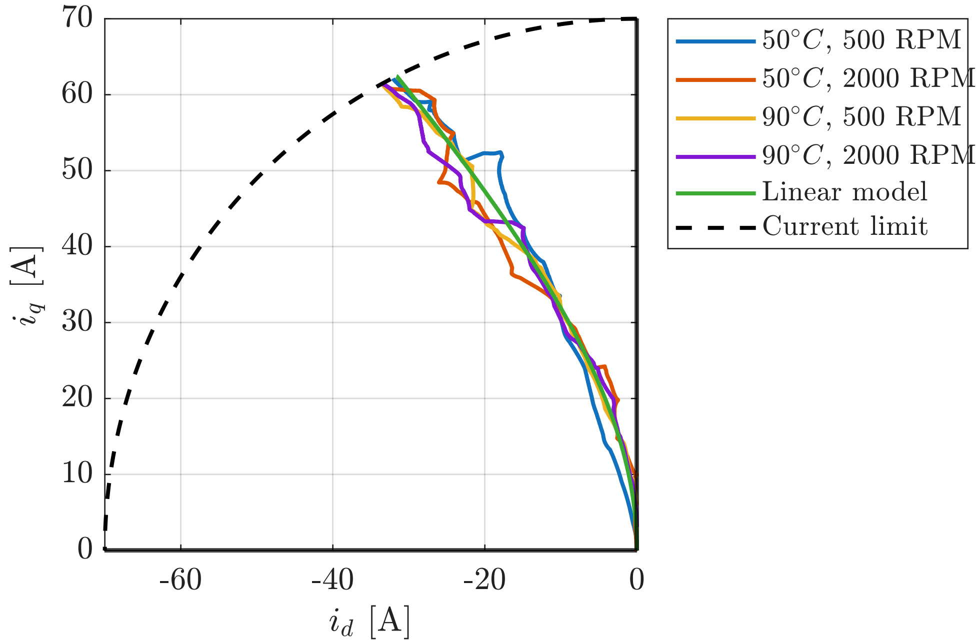

Figure 5.4: MTPA trajectories at highest and lowest speeds and temperatures.

With the accuracy reached for the MTPA trajectories, it is difficult to observe any meaningful differences between the different speeds and temperatures for the trajectories. In Figure 5.5, the torque achieved at each current magnitude along the four MTPA trajectories are presented.

Along the MTPA trajectories, the mappings show that produced torque increases linearly with the current magnitude, even at higher current levels. Although the differences are small, a reduction in torque is noticeable for both higher speeds and temperatures. The linear model consistantly predicts a larger torque for a given current magnitude. At lower current magnitudes, the linear model has a similar slope to the mapped cases. However, at higher currents, the linear model exhibits a super linear trend, increasing faster than strictly linear.

The derivatives of the curves in Figure 5.5, yields a torque constant, corresponding to the amount of torque produced for each ampere of current magnitude along the MTPA trajectory. This torque constant is presented as a function of the current magnitude in Figure 5.6 for the different cases and the linear model.

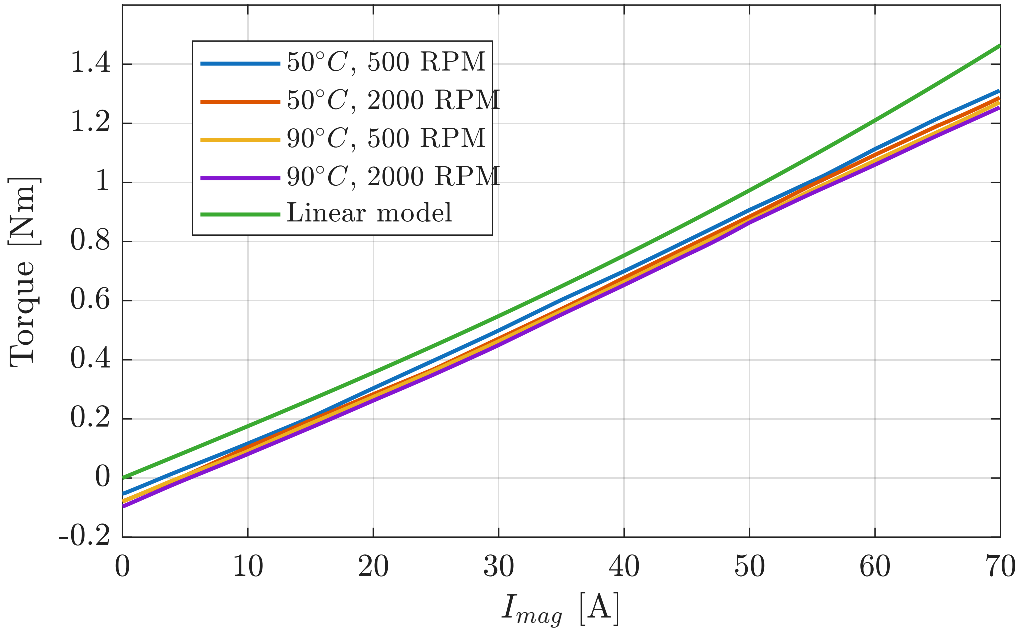

Figure 5.5: Torque at each current magnitude along MTPA trajectories.

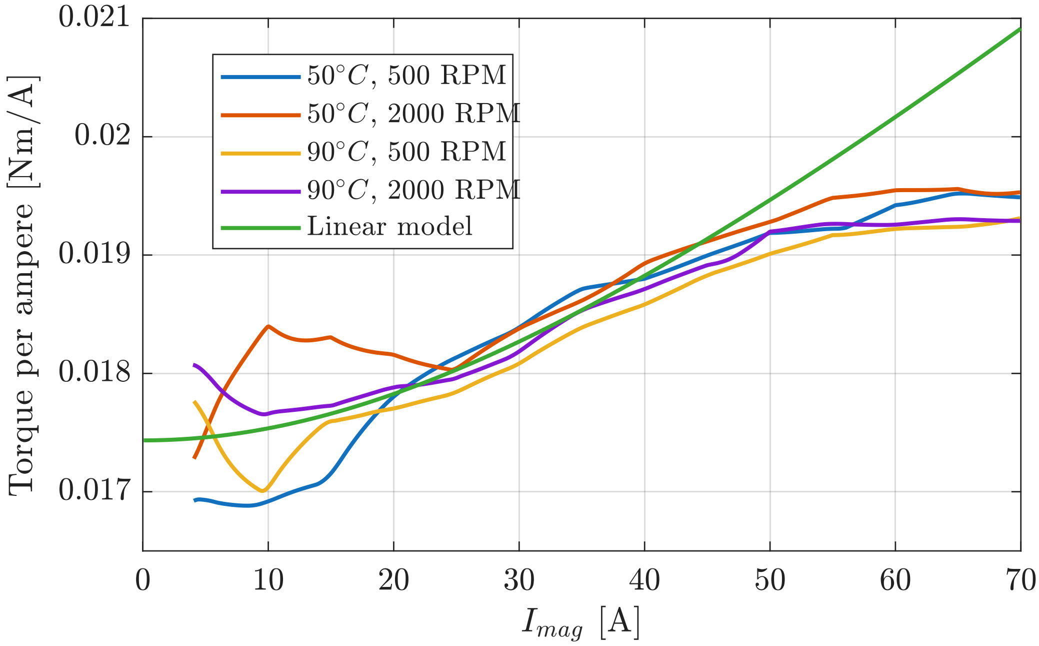

Figure 5.6: Torque constants as functions of the current magnitude.

For the current magnitudes in the interval 30 A to 40 A, where some torque is being produced while the machine is not saturated, there is a noticable difference between the linear model torque constant and the mapped cases. In this interval, the average differences between the mapped cases and the linear model are 0.000 120 Nm/A and 0.000 093 Nm/A for the case of 50 °C at 500 RPM and 2000 RPM respectively. For the 90 °C cases, the differences are −0.000 175 Nm/A at 500 RPM and −0.000 042 Nm/A at 2000 RPM. For higher current magnitudes the amount of torque produced per unit current stops increasing, indicating magnetic saturation. This non-linear behaviour clearly deviates from the linear PMSM model, where the torque constant continues increasing up to 0.0209 Nm/A. In contrast, the torque constants of the mapped machine cases stop increasing at 0.0195 Nm/A for 50 °C and 0.0193 Nm/A for 90 °C.

5.2 Flux linkage and inductance characteristics

5.2.1 Temperature dependence of R_s and Ψ_m

Table 5.1 shows the values of the stator resistance, R_s, and the permanent magnet flux linkage, Ψ_m, for different temperatures measured according to Section 3.3. As expected based on Section 2.5.3, R_s increases with temperature and Ψ_m decreases with temperature. From the measured data, the estimated temperature coefficient for the stator resistance was 0.270 %/°C, which is lower than the theoretical copper value of 0.393 %/°C [13]. This indicates that the measured increase in resistance with temperature is somewhat weaker than predicted by the ideal copper temperature dependence. The estimated temperature coefficient for the permanent magnet flux linkage was −0.0537 %/°C. This is also lower in magnitude than the typical NdFeB weakening of about −0.11 %/°C [14].

Table 5.1: Temperature-dependent stator resistance and permanent magnet flux linkage.

Temperature [°C]	R_s [Ω]	Ψ_m [Wb]
50	0.026573	0.008717
60	0.027340	0.008668
70	0.027949	0.008620
80	0.028612	0.008575
90	0.029300	0.008526

5.2.2 Flux linkage maps

The flux linkages, Ψ_d and Ψ_q, were calculated for each operating point using the voltage equations, (2.17) and (2.18), in steady state and are presented in the *dq*-plane in Figure 5.7 and 5.8. The temperature dependent stator resistance that was measured and presented in Table 5.1 was used for the calculation of the flux linkages.

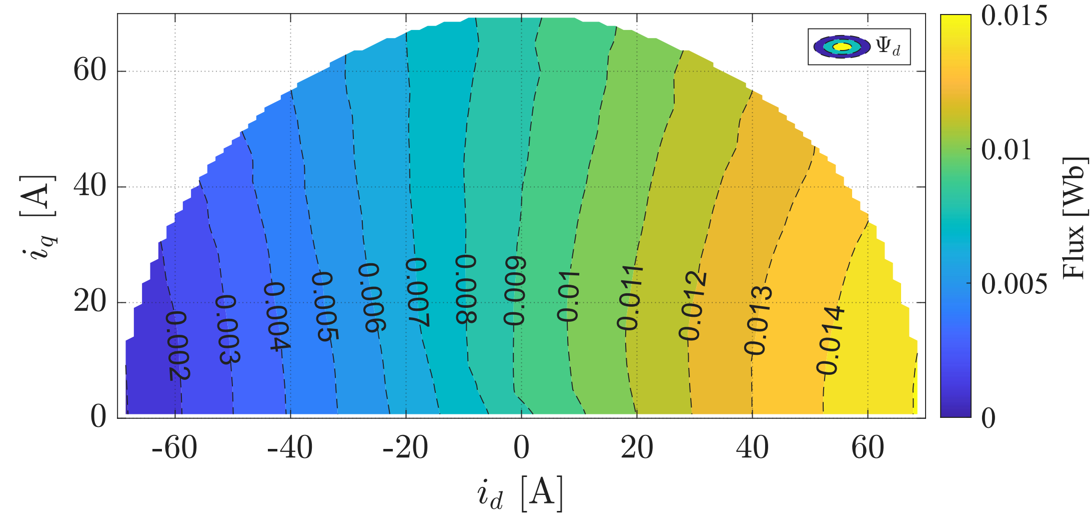

Figure 5.7: Flux in the d-axis for 1000 RPM and 50 °C.

The d-axis flux linkage in Figure 5.7 shows a strong dependency on the d-axis current component. The vertical ISO-curve at $i_d = 0$ corresponds to the permanent magnet flux linkage Ψ_m and acts as a constant offset in the d-axis flux linkage. The bending of the ISO-curves becomes more pronounced at higher positive current magnitudes, indicating cross-saturation between the d- and q-axes. The cross saturation is most visible in regions where both i_d and i_q are large, corresponding to operating points with high magnetic loading. For low current magnitudes, the flux linkage contours remain nearly straight and orthogonal to the d-axis, indicating weak magnetic coupling between the axes and approximately linear magnetic behaviour. At high positive d-axis currents, the spacing of the ISO-curves increase, indicating magnetic saturation.

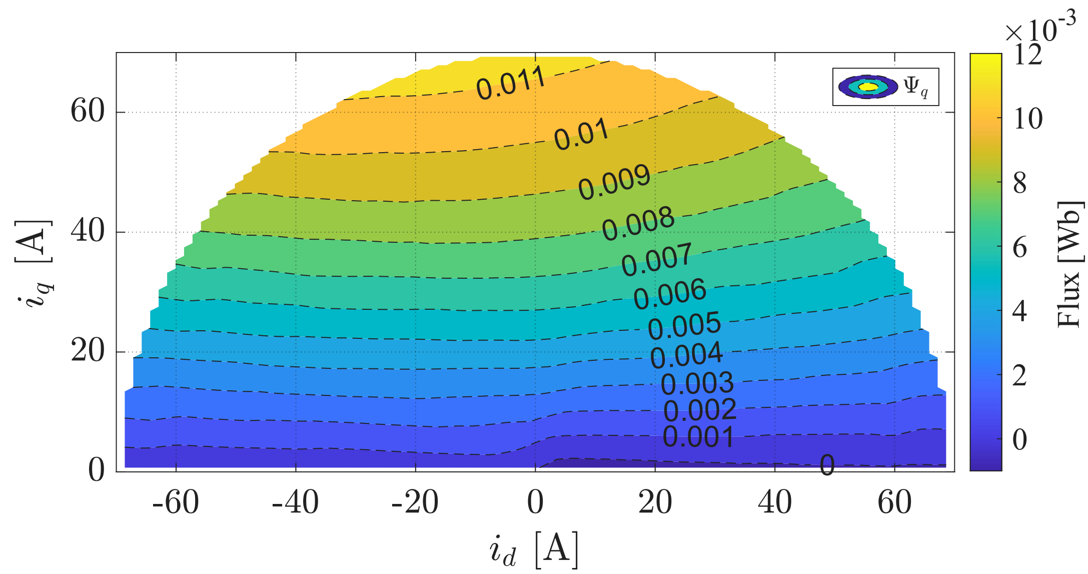

Figure 5.8: Flux in the q-axis for 1000 RPM and 50 °C.

The q-axis flux linkage in Figure 5.8 mainly depend on the q-axis current. For low current magnitudes, the relationship between Ψ_q and i_q is close to linear, resulting in nearly equally spaced ISO-curves. At higher q-axis currents the spacing increases, indicating saturation effects also in the q-axis flux linkage. Similarly to the d-axis flux linkage, cross saturation effects appear in the q-axis flux map. Variations in the i_d current cause the ISO-curves to bend, particularly at operating points with high i_q currents.

To investigate the flux linkage dependence on speed, point-wise difference maps between 500 RPM and 2000 RPM were calculated for the d- and q-axis flux linkages.

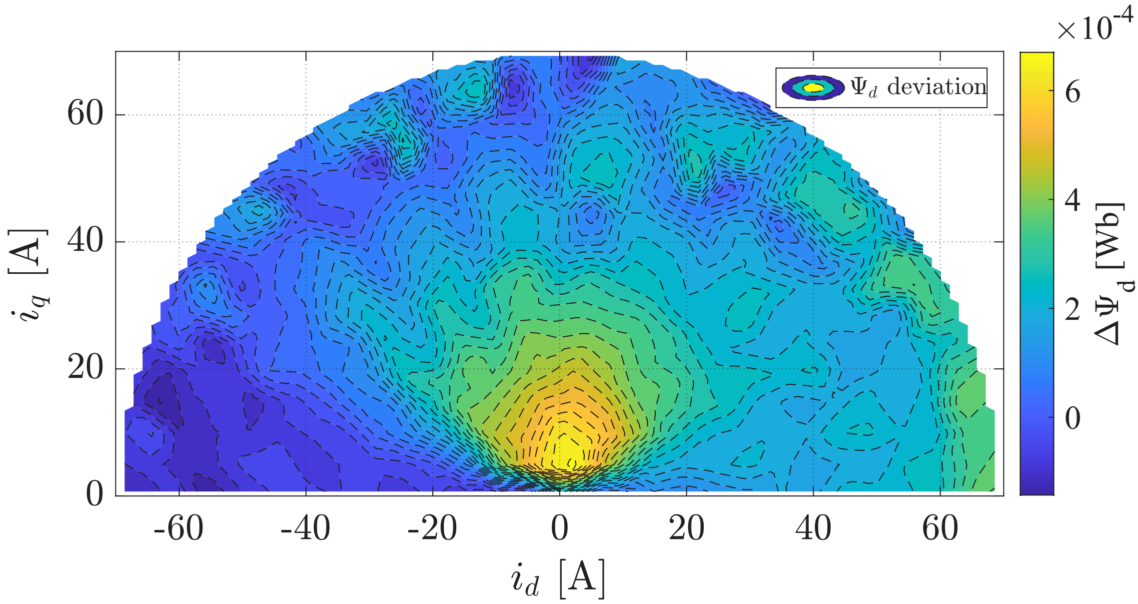

Figure 5.9: Flux deviation map for d-axis between 500 and 2000 RPM at 50 °C.

In the d-axis deviation map, it is clear that the largest difference occurs close to the origin. Apart from the significant difference for low current magnitudes, a larger difference is visible for positive d-axis current components than for negative i_d currents.

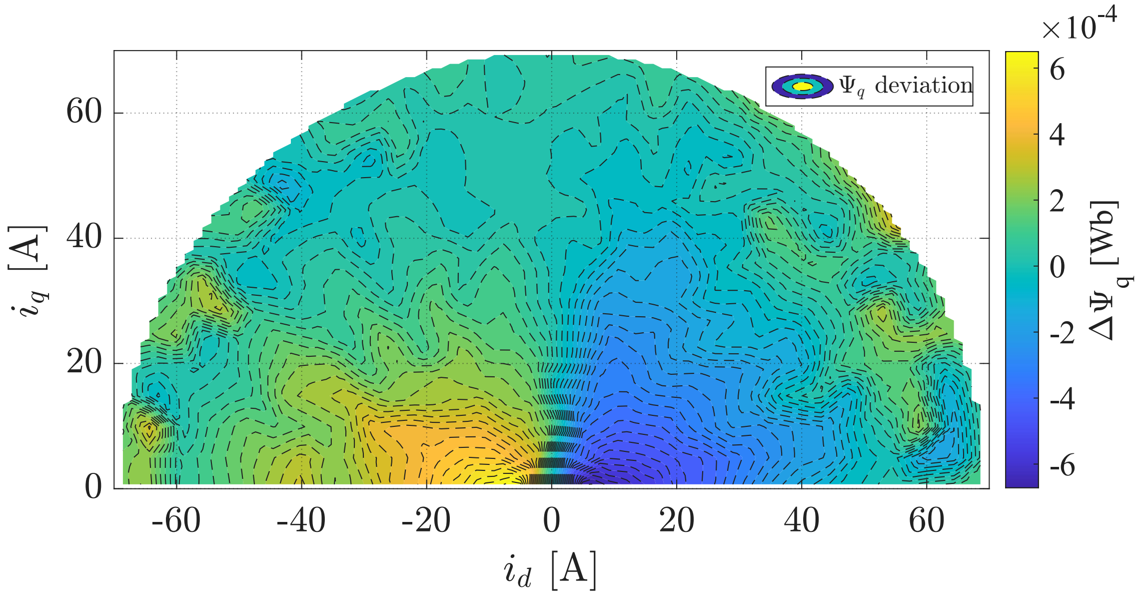

Figure 5.10: Flux deviation map for q-axis between 500 and 2000 RPM at 50 °C.

Likewise to the d-axis flux linkage, in the q-axis flux deviation map shows most activity close to the origin of the current plane. A vertical line of small deviations separate areas of large positive deviations to the left from large negative deviations on the right.

To investigate the temperature dependence of the flux linkages, the map at 90 °C was subtracted from the one at 50 °C, at a speed of 2000 RPM. The d-axis flux linkage difference map is presented in Figure 5.11.

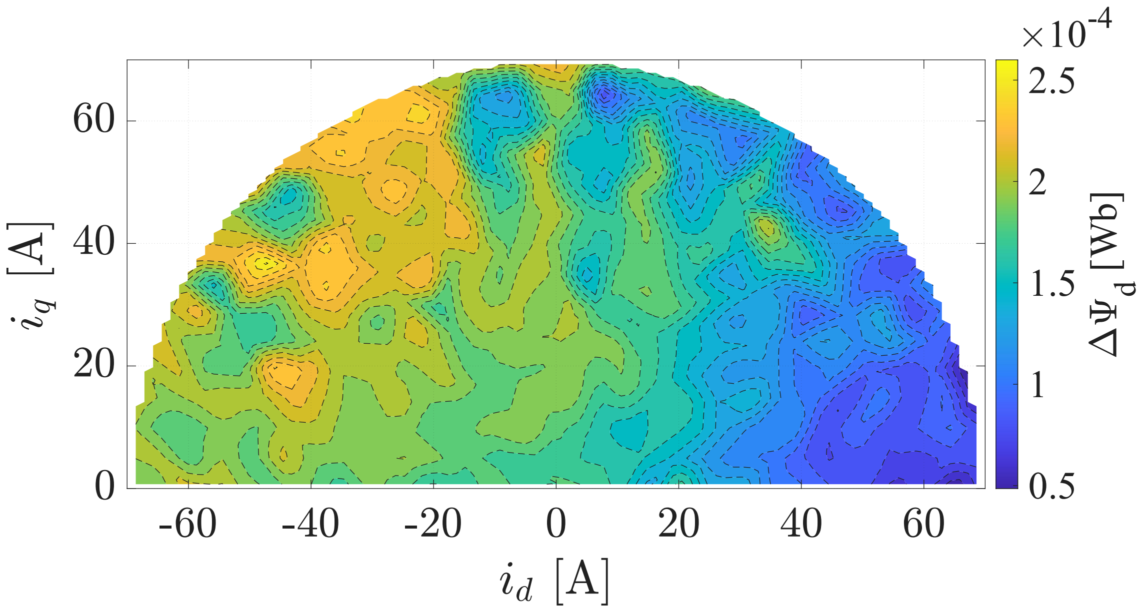

Figure 5.11: Flux deviation map for d-axis between 50 and 90 °C at 2000 RPM

.

The deviation map for the d-axis flux linkage shows dependence on temperature, with a general reduction at the higher temperature of 90 °C compared to 50 °C. A larger reduction in Ψ_d can be seen for negative d-axis currents in the left half plane, while the reduction is smaller in the right half plane, where i_d is positive. Similarly, the deviation map for the q-axis flux linkage is presented in 5.12.

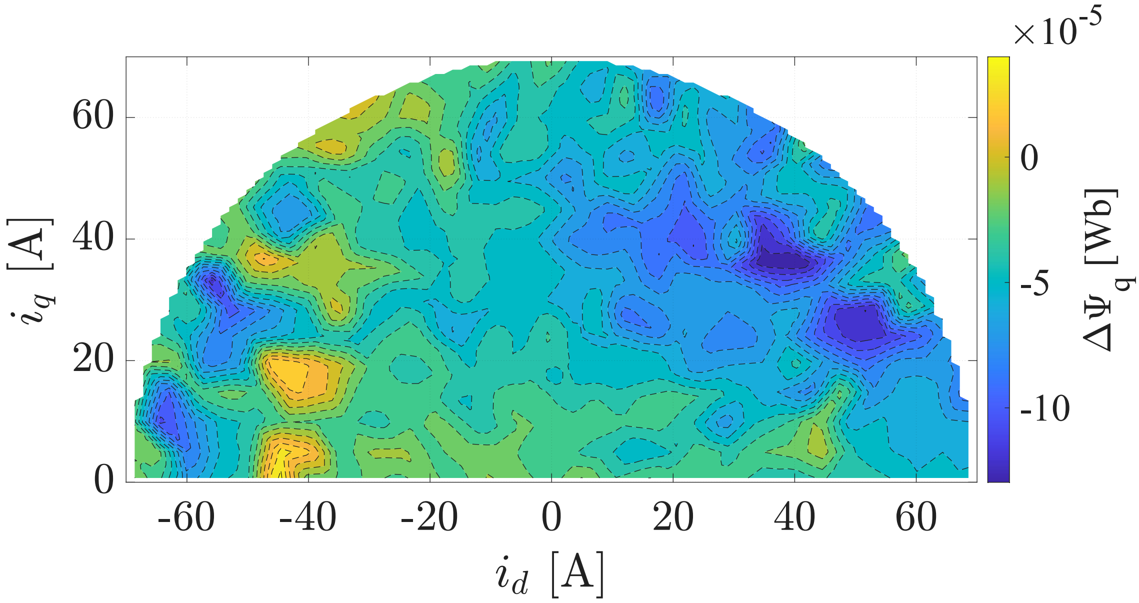

Figure 5.12: Flux deviation map for q-axis between 50 and 90 °C at 2000 RPM

.

For the q-axis flux linkage, a slight increase can be seen for higher temperatures. However, the deviation is smaller and more evenly spread across the current plane, apart from some spots of slightly higher deviation. This indicates that the q-axis flux linkage is less dependent on temperature compared to the d-axis flux linkage.

5.2.3 Inductance characteristics

To illustrate the inductance characteristics of the machine based on the calculated flux linkage maps, the inductances L_d, L_q, L_{dq} and L_{qd} were calculated based on (2.42) and (2.43) from measurement data at 2000 RPM and 50 °C. This was done by numerically evaluating the partial derivatives of the d- and q-axis flux linkages with respect to the d- and q-axis currents. In Figure 5.13, L_d is shown as the derivative of Ψ_d with regard to i_d for different values of constant i_q. It can be seen that for negative i_d, where the induced flux counteract the permanent magnet flux linkage, and $i_q = 0$ the inductance is approximately constant between 0.11 mH to 0.12 mH. While for positive i_d, L_d reduces quickly to below 0.06 mH for $i_d > 60$ A. Cross saturation effects can also be seen clearly where $i_q = 60$ A causes L_d to drop from 0.12 mH to 0.09 mH at $i_d = 0$ A. At $i_q = 30$ A the cross saturation effect is not as clear but still visible when i_d is between -15 A and 60 A.

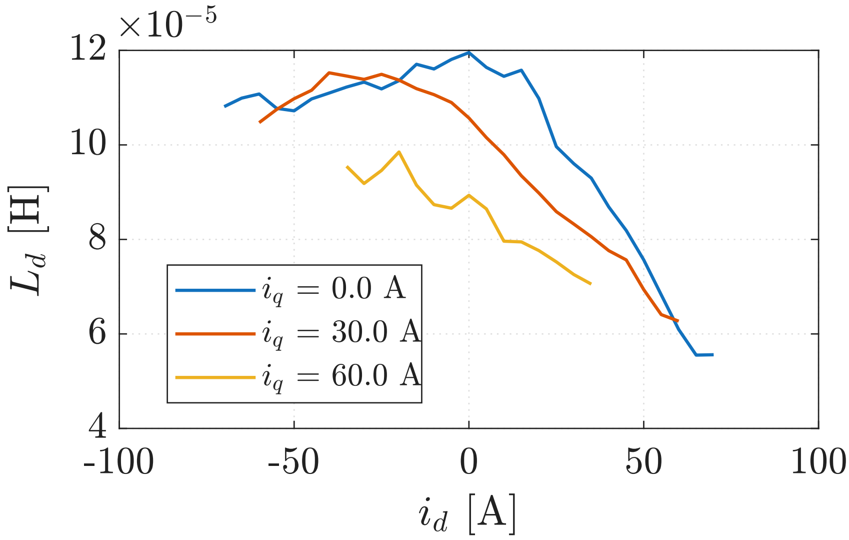

Figure 5.13: L_d variation with regard to i_d for constant values of i_q.

In Figure 5.14, L_q is shown as the derivative of Ψ_q with regard to i_q for different values of constant i_d. At $i_q < 20$ A, L_q is around 0.23 mH for $i_d = 0$. As i_q increases past 20 A saturation starts to occur gradually, with the fastest reduction in L_q at 30 to 40 A and L_q dropping to 0.09 mH at $i_q = 70$ A. The cross saturation effect of i_d on L_q can be seen for $i_d = 60$ A where L_q is 0.19 mH for $i_q = 0$ A.

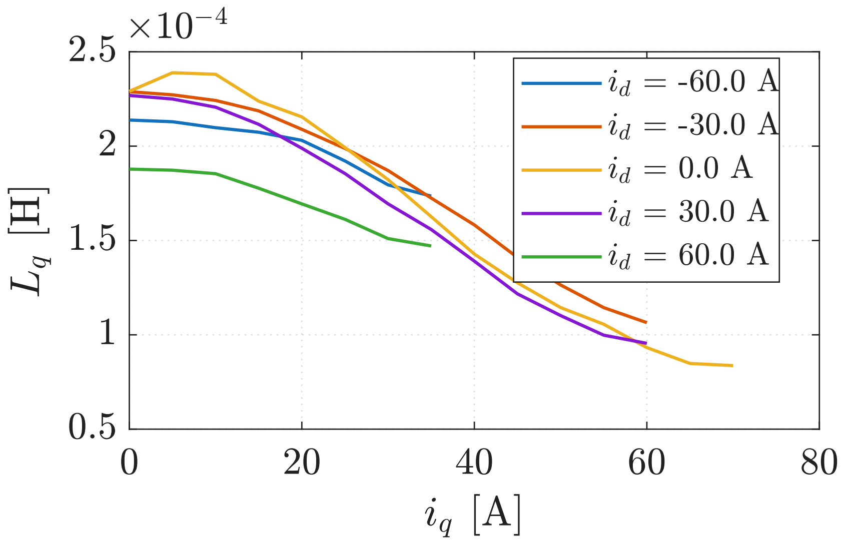

Figure 5.14: L_q variation with regard to i_q for constant values of i_d.

In Figure 5.15, L_{dq} is shown as the derivative of Ψ_q with regard to i_d for different values of constant i_q. L_{dq} is approximately zero for $i_q = 0$ A, except when i_d is close to zero where it reaches -0.05 mH. For positive i_d and i_q, L_{dq} is negative with a minimum at -0.035 mH, meaning that the q-axis flux generated by the d-axis current opposes the q-axis flux generated by the q-axis current. However for negative i_d, L_{dq} is still slightly negative in some areas meaning that i_d creates a q-axis flux in the same direction as i_q, but is positive for $i_q = 30$ with a maximum at 0.015 mH.

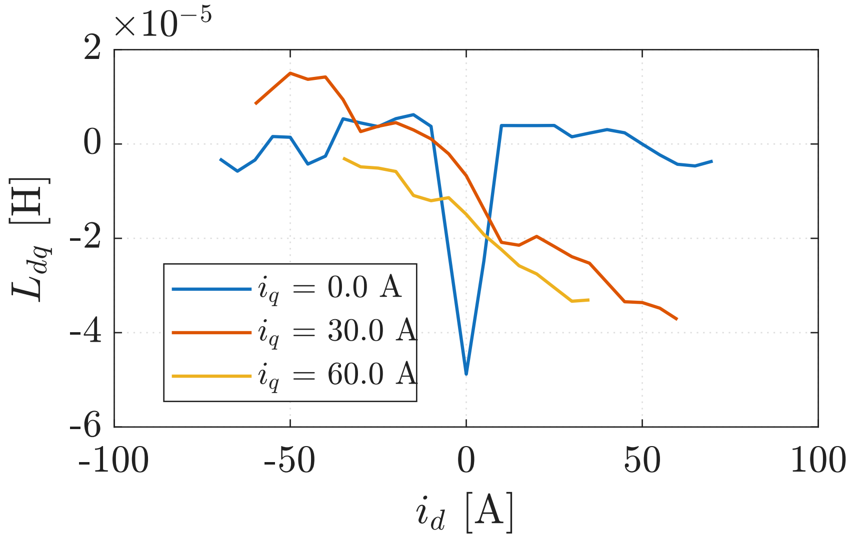

Figure 5.15: L_{dq} variation with regard to i_d for constant values of i_q.

In Figure 5.16, L_{qd} is shown as the derivative of Ψ_d with regard to i_q for different values of constant i_d. For $i_d = 0$ A, L_{qd} is slightly negative except for low values of i_q meaning that the d-axis flux is reduced by the q-axis current. For $i_d < 0$ A, L_{qd} is positive with a maximum at 0.02 mH and for $i_d > 0$ A, L_{qd} is negative with a minimum at -0.025 mH.

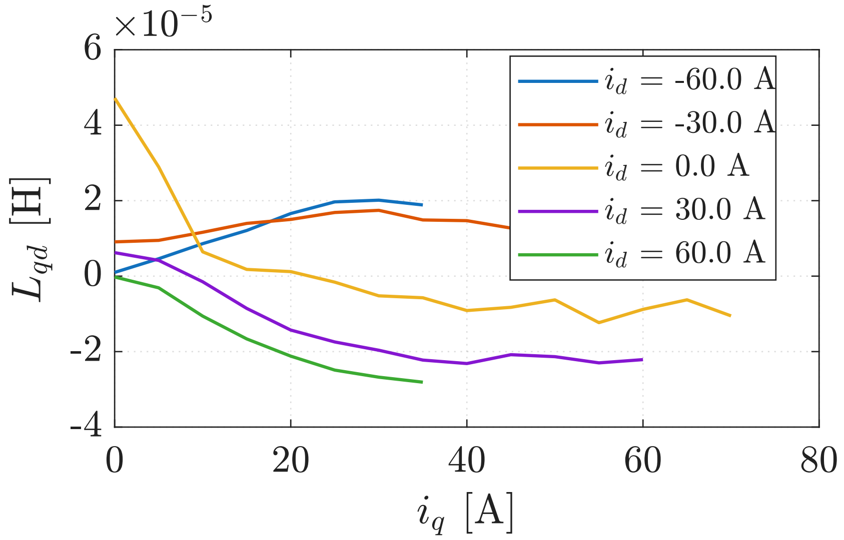

Figure 5.16: L_{qd} variation with regard to i_q for constant values of i_d.

The temperature and speed dependence of L_d, L_q, L_{dq} and L_{qd} was also evaluated. In Figure 5.17 L_d is shown based on measurements at 500 and 2000 RPM, as well as 50 and 90 °C. Clearly the temperature makes very little difference and the speed only makes the measurements more noisy at 500 RPM compared to 2000 RPM. This behaviour was observed for the other inductances and mapping cases as well.

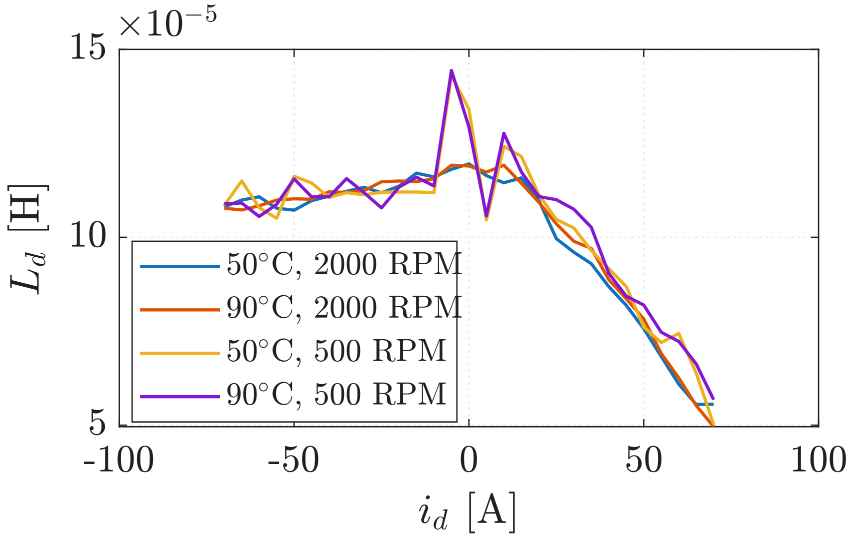

Figure 5.17: L_d variation with regard to i_d with $i_q = 0$ for different speeds and temperatures.

5.3 Voltage constraints in the current plane

Based on the flux linkage data extracted from different speed and temperature mapping cases, the voltage limit ellipse could be calculated for any machine speed at the DC-link voltage of 12 V using (2.38). Voltage limit ellipses were calculated for the same set of machine speeds for each mapping dataset and the linear machine model in order to compare the flux linkage mappings for different speeds and temperatures. In Figure 5.18, four different ellipses are presented at each machine speed, calculated from the datasets at 500, 1000, 1500 and 2000 RPM respectively, all at a temperature of 50 °C.

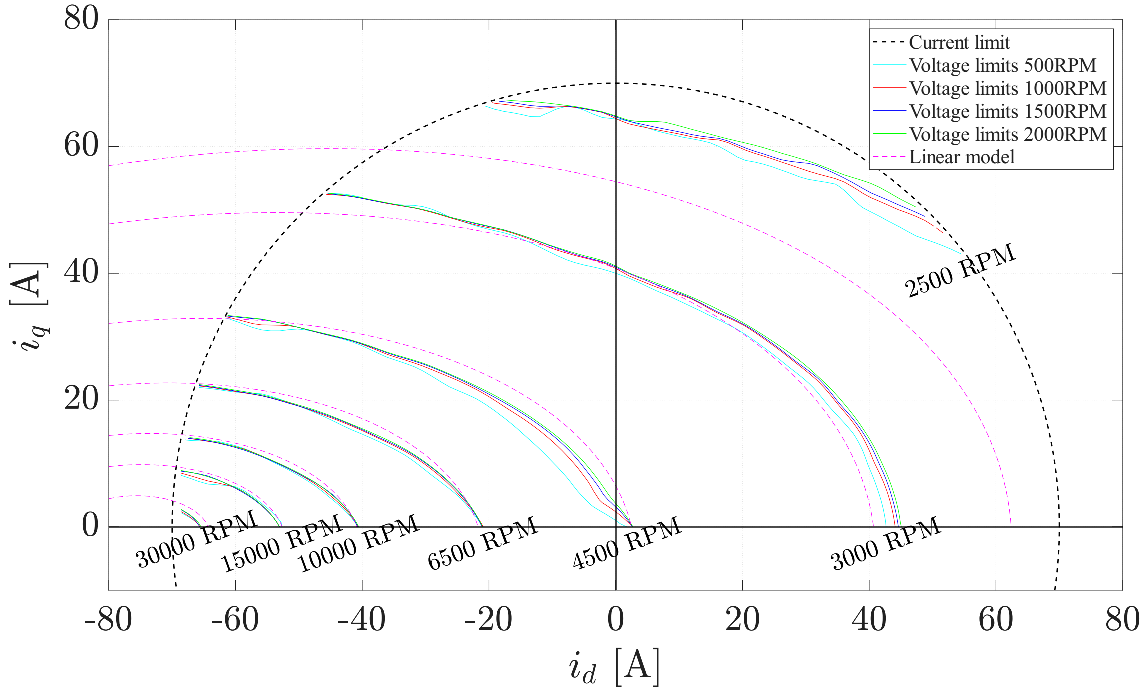

Figure 5.18: Voltage limit ellipses for different speeds at 50 °C.

The voltage ellipses decrease in size with increasing rotational speed, meaning that the set of achievable current vectors shrinks. The voltage limit ellipses for the mapped cases intersect the current limit circle at a speed of approximately 2400 RPM. This means that below this speed, all current vectors within the current limit circle are achievable with the DC-link voltage of 12 V.

The ellipses calculated from mappings at different speeds follow similar paths. A small difference can be seen, where higher speeds seem to have slightly larger ellipses, indicating lower voltage requirements for the same currents. It is also clear that the smaller absolute voltage values during measurement of the 500 RPM case leads to more jagged ellipses compared to the higher speed mappings.

The linear model ellipses are similar to the mapped counterparts for higher speeds in the left half plane, but differs considerably for 2500 RPM. For 3000 RPM, the difference is most significant for the highest values of the *d*-axis current, as well as toward the current limit circle in the left half plane. For the case of 2500 RPM, where both the *d*- and *q*-axis currents are large, there is a significant difference along the entire visible ellipse segment.

In Figure 5.19, two different ellipses are presented at each machine speed, calculated from the datasets at 50 and 90 °C respectively, both at 2000 RPM. The mapping cases at 2000 RPM are chosen since they provide the smoothest voltage ellipses.

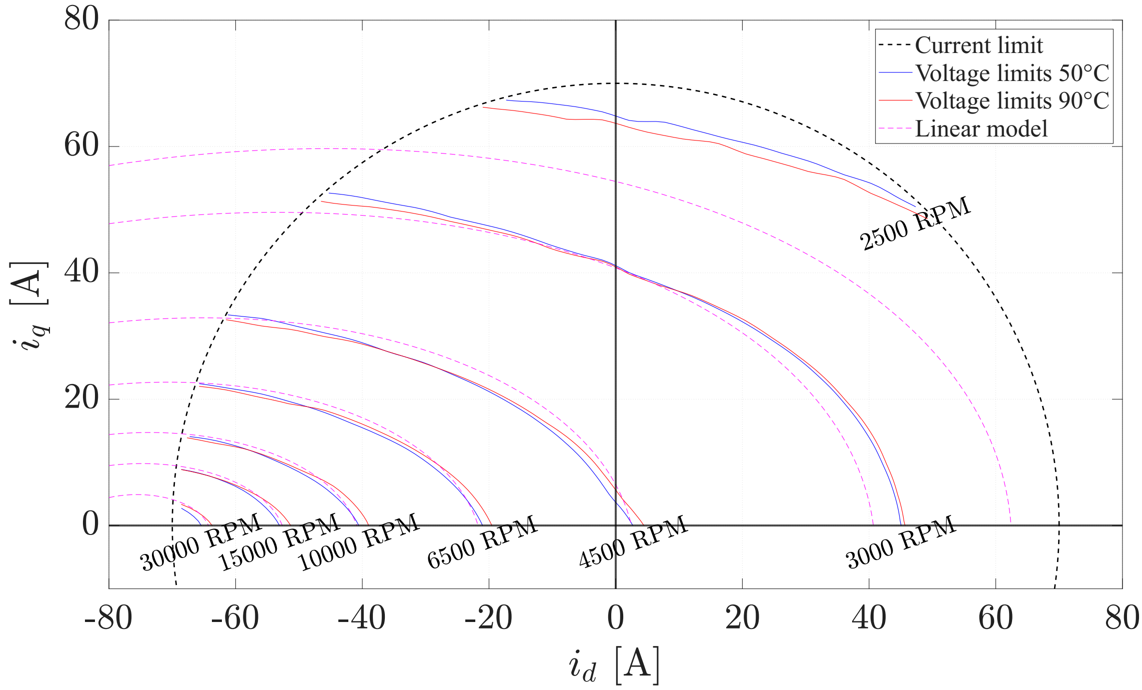

Figure 5.19: Voltage ellipses for 500 and 2000 RPM at 50 and 90 °C.

The comparison between the temperature cases behave differently in different areas of the current plane. The case of 50 °C is the most limiting closer to the *d*-axis. Further from the *d*-axis, where high current magnitudes are reached, without deep field weakening, the case of 90 °C is the most limiting.

The MTPV trajectory, where the maximum achievable torque for a certain voltage is reached, is located at the points where the constant torque curves tangent the voltage limit ellipses. For this drive system, these points are found outside of the current limit circle, which means that MTPV operation at a DC-link voltage of 12 V will not be reached without overloading the drive system.

5.4 Efficiency mapping and optimal trajectories

The efficiency of the machine was determined across the studied operating region for the base case of 1000 RPM and 50 °C and is illustrated in Figure 5.20.

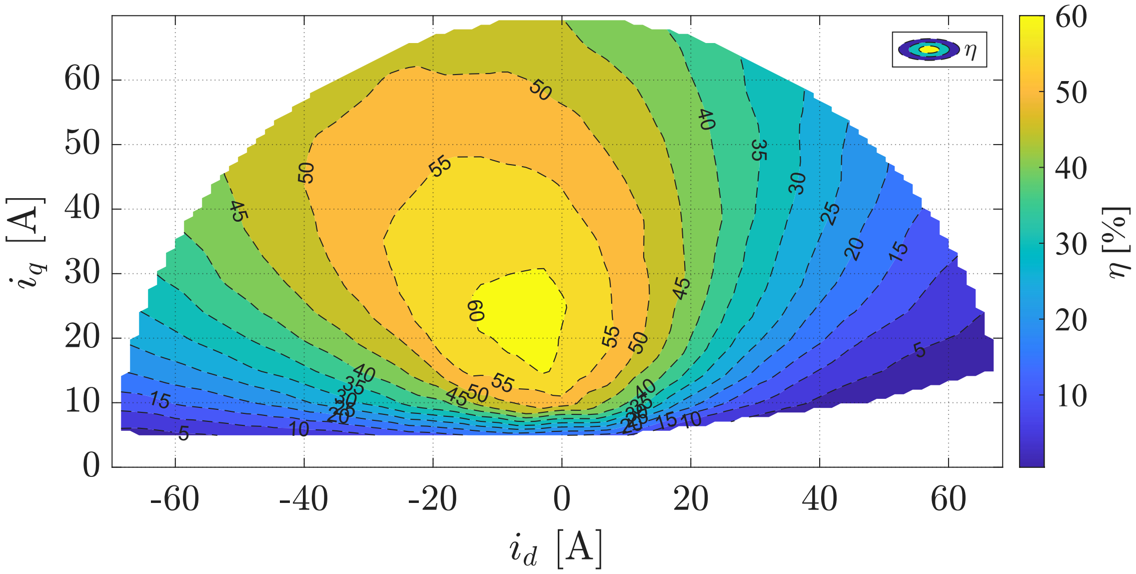

Figure 5.20: Machine efficiency at 1000 RPM and 50 °C.

The efficiency shows a clear dependence on the selection of the operating point in the current plane. At low current magnitudes, the efficiency remains relatively low due to the small mechanical output power in relation to the machine losses. As the current magnitude increases, particularly in the q-axis, the machine efficiency increases rapidly and reaches its maximum value in the low to medium torque range. The highest efficiencies are observed for operating points with positive q-axis currents, and slight negative d-axis currents, approximately corresponding to the MTPA region. For current angles far from the MTPA region, the efficiency of the machine is greatly reduced. Additionally, the efficiency of the machine decreases as currents reach high magnitudes.

To investigate the influence of rotational speed on the efficiency characteristics, the efficiency map at 500 RPM was subtracted from the one at 2000 RPM, both at 50 °C. This deviation map is presented in Figure 5.21.

A systematically higher efficiency can be observed in large parts of the current plane for 2000 RPM compared to 500 RPM. The increase in efficiency with speed is significant, and largest in the regions of high torque production, reaching a maximum of 30 percentage points higher for 2000 RPM. The efficiency improvement is less pronounced at lower current magnitudes and high current angles, since the mechanical output power is low compared to the losses in these areas.

The impact of temperature variations to machine efficiency was investigated by comparing the efficiency maps at 50 °C and 90 °C. The deviation map is shown in Figure 5.22.

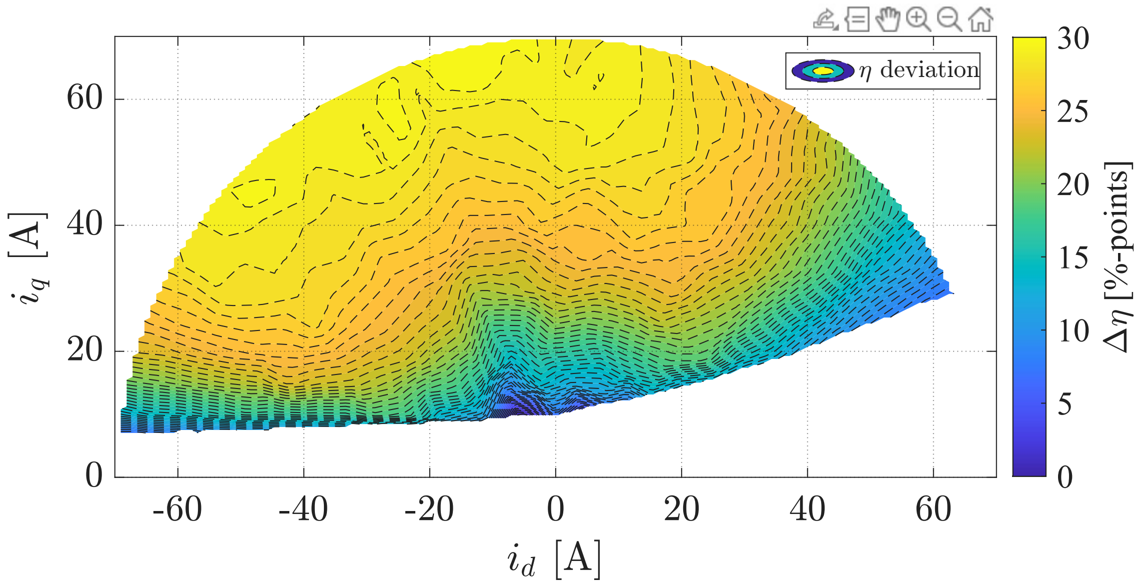

Figure 5.21: Efficiency deviation between 2000 RPM and 500 RPM at 50 °C.

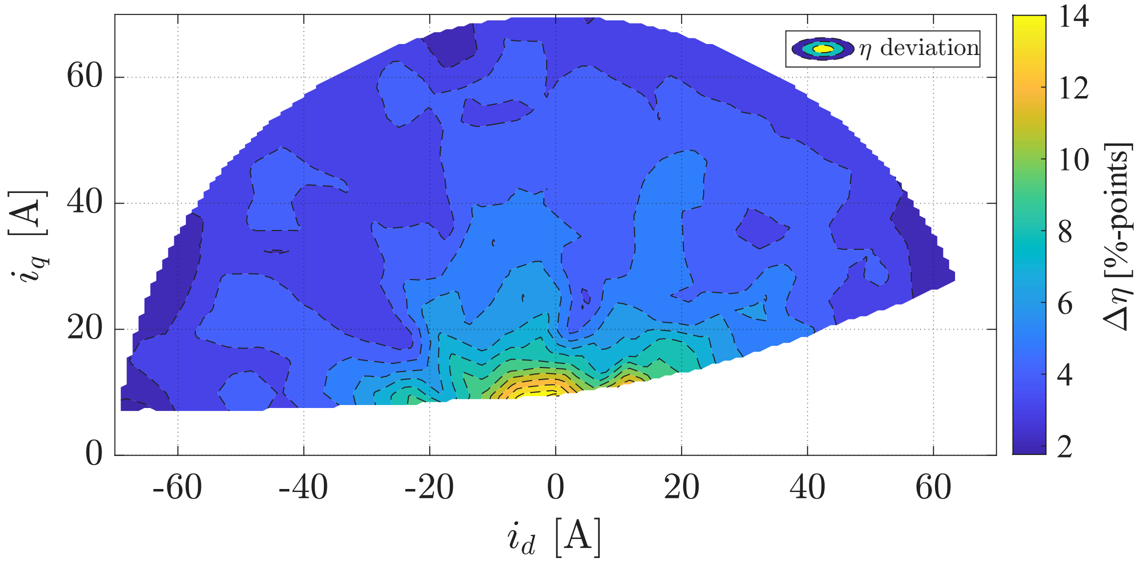

Figure 5.22: Efficiency deviation between 50 °C and 90 °C at 1000 RPM.

Increasing temperatures cause a systematic reduction of the machine efficiency across the entire operating region. The largest efficiency deviations are observed close to the origin of the current plane, where the produced mechanical output power is low. At higher current magnitudes, the efficiency deviation between the temperature cases decrease.

5.4.1 Trajectory comparison

To evaluate the impact of using data driven current trajectories, four different current reference strategies were compared.

- Fixed current angle
- Analytical MTPA based on the linear PMSM model
- Mapped MTPA extracted from measured torque maps
- Mapped Maximum Torque Per Watt (MTPW) extracted from torque maps and calculated input power

The fixed current angle was chosen so that the operating point of maximum torque aligned with the analytical solution from the linear PMSM model, (2.35). The presented points for the mapped MTPA are extracted from the torque data by finding the current vector with the smallest magnitude at each constant torque level. A function curve is fitted to the extracted points, resulting in the mapped MTPA trajectory. The resulting MTPA trajectories in the current plane are presented in Figure 5.23.

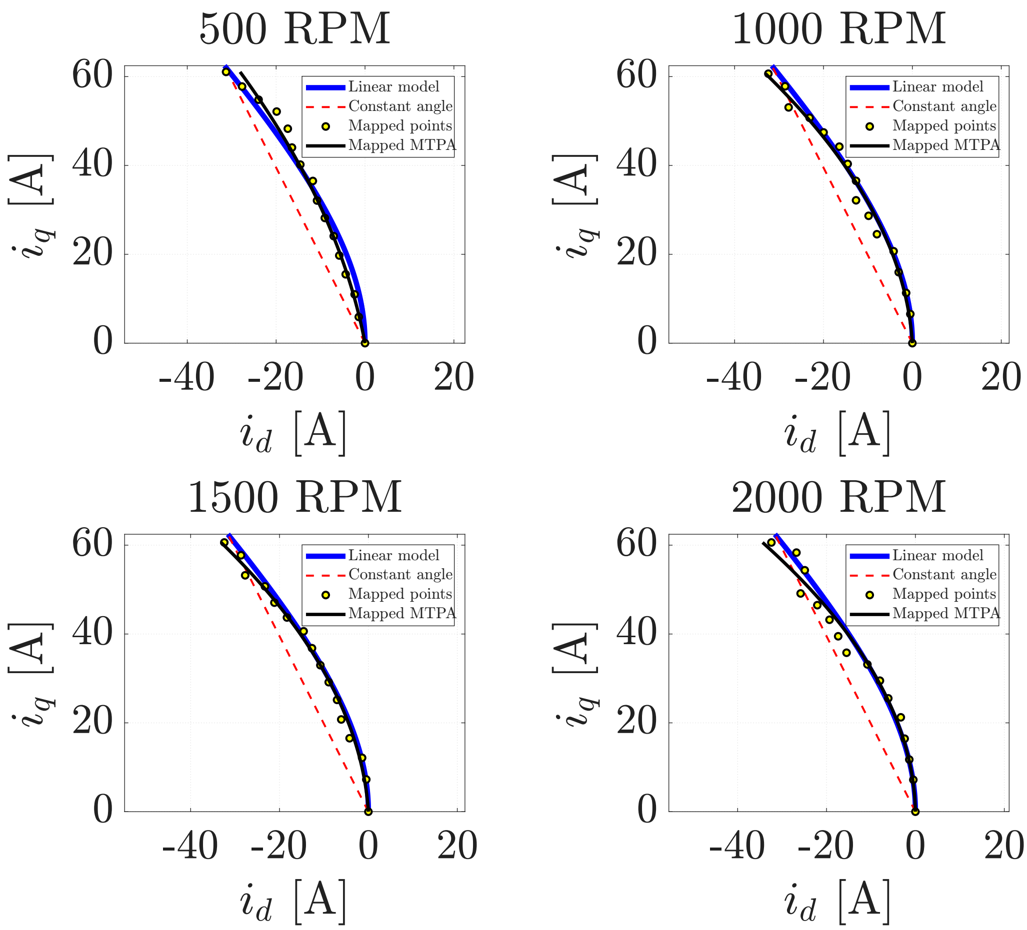

Figure 5.23: MTPA trajectories for different speeds at 50 °C.

As observed, the linear model analytical MTPA and the mapped MTPA follow similar paths. A slight shift along the negative d-axis can be observed for the mapped MTPA trajectories, especially at higher speeds. The constant angle trajectory deviates from both curves across the entire operating range, apart from the operating point of maximum torque. For the studied machine, the constant MTPA angle was approximately 26.8° from the positive q-axis.

To quantify the energy efficiency of each strategy, the fixed angle, analytical and mapped MTPA trajectories where determined alongside the mapped MTPW trajectory. MTPW is determined from the mapped torque data and the input power, calculated from (2.23), by finding the current vector with the lowest input power at each constant torque level. In order to compare them, function curves were fitted to the measured points, and the results are overlayed on the efficiency map in Figure 5.24. The speed was chosen to 2000 RPM for the comparison, in order to maximize iron losses and increase the possible differences between the trajectories.

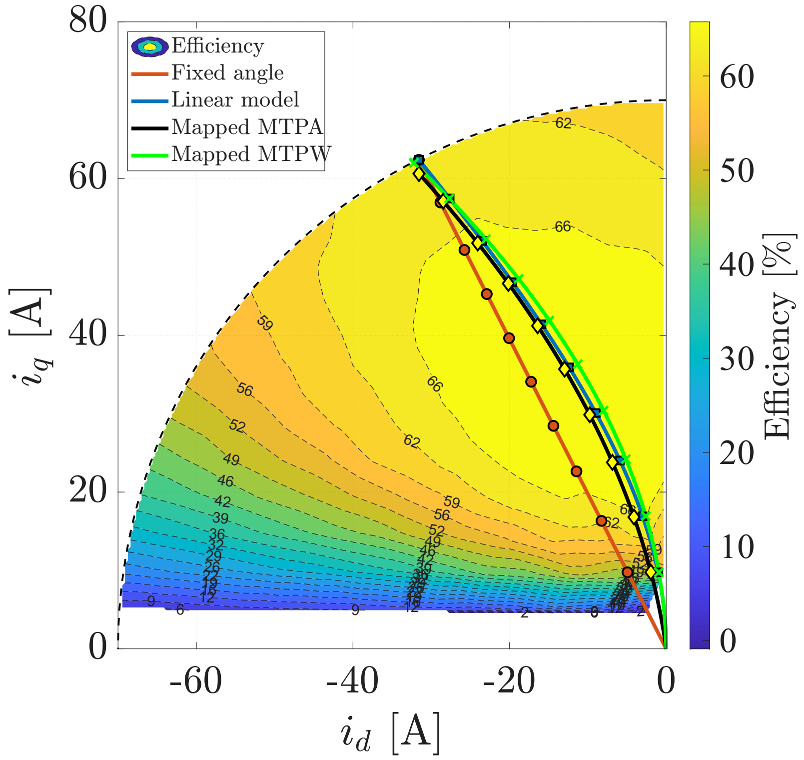

Figure 5.24: Trajectories overlayed on efficiency map at 2000 RPM and 50 °C.

The efficiency values were extracted for 10 equally spaced points between zero and maximum achieved torque for all trajectories. The resulting efficiency values are presented in Table 5.2. The bottom row shows the mean efficiency of the different trajectories, calculated as the mean of the shown values in each column.

Table 5.2: Comparison of efficiencies of different current selection methods.

Torque (Nm)	Fixed Angle	Analytical MTPA	Mapped MTPA	Mapped MTPW
0.1	47.7	52.4	51.2	52.5
0.2	62.8	65.8	65.4	65.9
0.4	67.1	67.5	67.4	67.6
0.5	68.4	68.9	68.8	69.0
0.6	68.6	68.7	68.7	68.8
0.8	67.9	68.1	68.1	68.1
0.9	67.1	67.2	67.2	67.2
1.0	66.3	66.2	66.2	66.2
1.2	64.4	64.7	64.5	64.6
1.3	62.7	62.7	63.0	62.7
Mean	**64.30**	**65.22**	**65.05**	**65.26**

Clearly, the difference between the different trajectories is small. The mapped MTPW yields the highest mean efficiency, followed by the analytical MTPA and mapped MTPA, while the fixed angle has the lowest mean efficiency. There is a slight increase in efficiency when moving from fixed angle MTPA to the other trajectories, particularly in the low torque region. However, between the analytical MTPA, mapped MTPA and mapped MTPW, the difference is negligible. This indicates that the classical solution of following the MTPA trajectory rather than the MTPW trajectory yields close to optimal efficiency in the current vector selection at the speeds measured in this work.

5.5 LUT-based machine model

To assess the accuracy of the constructed machine model, the simulation outputs were compared to the captured datasets for the different mapping cases. The comparison was conducted in steady-state across the cases of highest and lowest speeds and temperatures.

For each mapping dataset, measured d- and q-axis voltages were extracted for each measured operating point and fed into the Simulink model. The resulting steady-state currents and torque from the simulation output were extracted and compared to the corresponding current and torque values measured for that operating point. For each mapping dataset, the mean and maximum deviations in currents and torque were determined and are presented in Table 5.3.

Table 5.3: Model errors compared to different mapping cases.

Operating case	i_d Error [A] (Mean / Max)	i_q Error [A] (Mean / Max)	T_e Error [Nm] (Mean / Max)
2000 RPM, 50 °C	0.355 / 7.694	0.285 / 3.843	0.087 / 0.179
500 RPM, 50 °C	0.867 / 5.499	0.834 / 4.181	0.075 / 0.160
2000 RPM, 90 °C	1.349 / 10.204	1.143 / 5.696	0.120 / 0.280
500 RPM, 90 °C	3.264 / 8.736	3.075 / 8.743	0.141 / 0.303

As expected, the errors are smallest for the case of 2000 RPM and 50 °C since this was the dataset used to generate the model lookup-tables. The mean current errors, dependent on the flux linkage lookup tables, for this case remain well below 0.5 A. The mean torque error amounts to 0.087 Nm, which is close to the value used in the compensation of the zero-torque curve discussed in Section 4.1. Without this compensation, the model error for the torque would be close to zero for this mapping case. As the model is compared to datasets collected at lower speeds and higher temperatures, the accuracy decreases as the operating conditions move further from the ones used in model lookup-table generation. The case of 500 RPM and 90 °C has the highest errors, with mean current errors above 3 A and a mean torque error of 0.141 Nm.

5.6 Simulation of data-driven current selection

The LUT-based current selection method was tested for a number of cases to assess the impact on control performance and show the selected current vector references. The test cases, described in Section 4.3, push the drive system into different limitations, evaluating what trajectories the current references follow.

The first case, where the load torque is ramped up to the maximum torque of the machine while operating at a constantly low speed is presented in Figure 5.26.

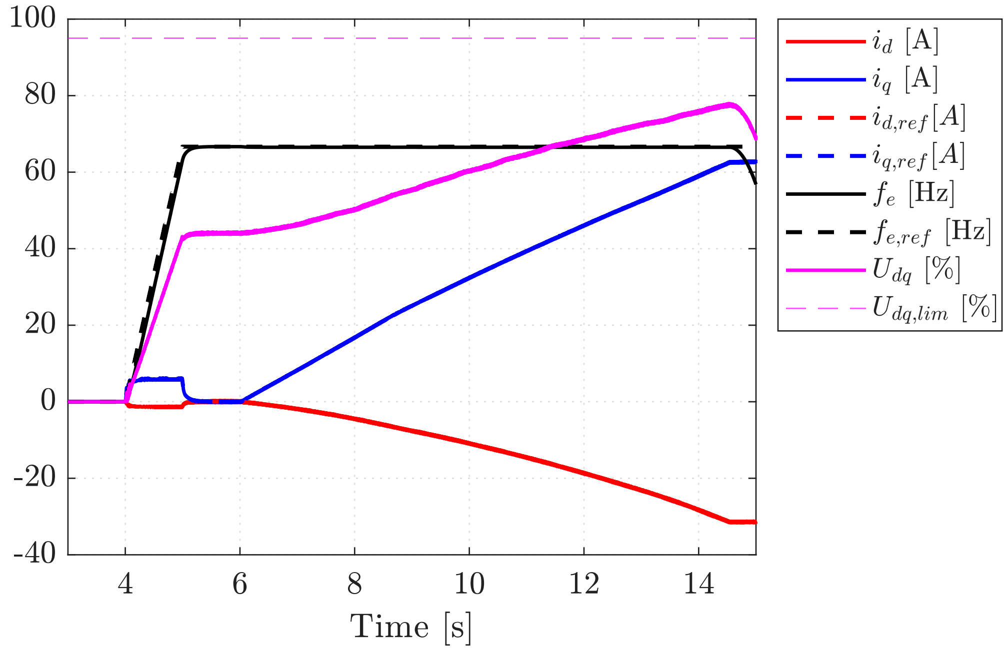

Figure 5.25: Dynamic performance for test case 1.

The dynamic performance show that the references are met for both speed and currents during the majority of the load ramp. At approximately 14.5 s, the currents flatten out and the speed drops. This is a result of the current limit being reached where the maximum torque is produced, while the continued increase in load torque causes a reduction in speed. The voltage utilization remains below 80 % and no voltage limitation is reached. In Figure 5.26, the selected current references are presented in the dq-plane.

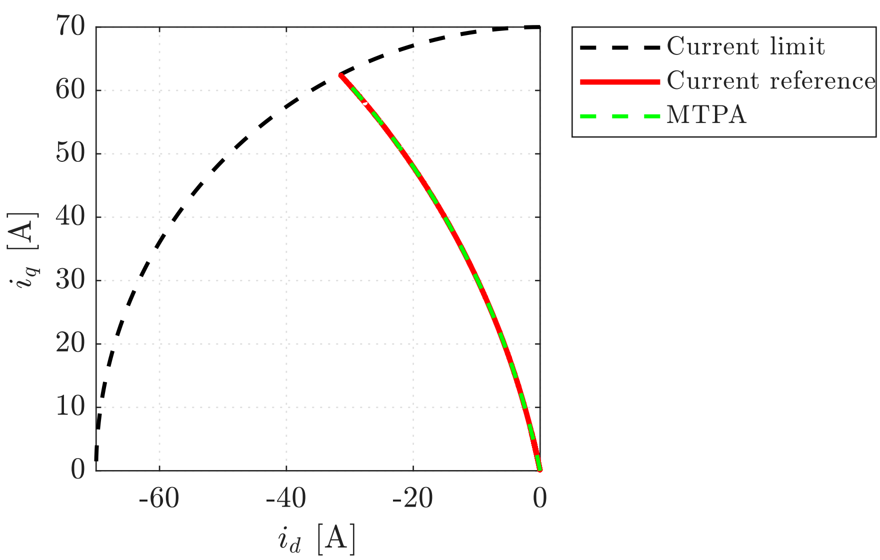

Figure 5.26: Current reference trajectory for case 1.

The selected current references follow the MTPA trajectory, from zero torque up to the maximum achievable torque at the current limit as the load ramps up. It is clear that no voltage limitation is reached, and no field weakening performed, since the current references never deviate from the MTPA trajectory, providing the highest torque for the given current magnitude.

In the second test case, the behaviour under voltage limitation is investigated. The speed reference is held high, while the load torque ramps up. The dynamic performance is presented in Figure 5.27.

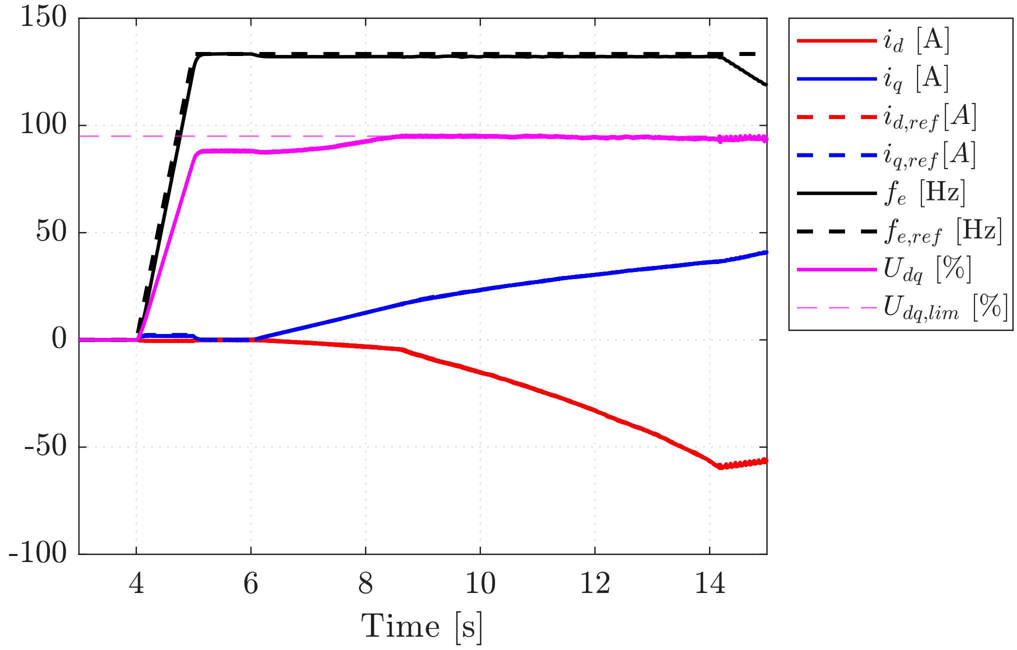

Figure 5.27: Dynamic performance for test case 2.

Similarly to the first test case, both the speed and current references are met until the very end of the sequence, where the speed drops. Contrary to the first case, a voltage limitation is reached as the load torque ramps up due to the higher electrical frequency of 133 Hz corresponding to a mechanical speed of 4000 RPM.

In Figure 5.28, the selected current references are presented, along with the MTPA trajectory, the voltage limit ellipse for 4000 RPM and two constant torque curves. During acceleration and while the load remains low, the machine is not limited by voltage and operates along the MTPA trajectory. As the load increases and the voltage limit is reached, the selected current references follow the voltage limit ellipse for 4000 RPM in the *dq*-plane. The breaking point, where the references deviate from MTPA, is located at the intersection point between the MTPA curve and this voltage limit ellipse. As the current limit is reached, the highest torque of 0.98 Nm for the available voltage is achieved and the speed starts to decrease, since the load torque continues to increase. This slight decrease reduces the voltage demand, and the current references move up in torque along the current limit circle.

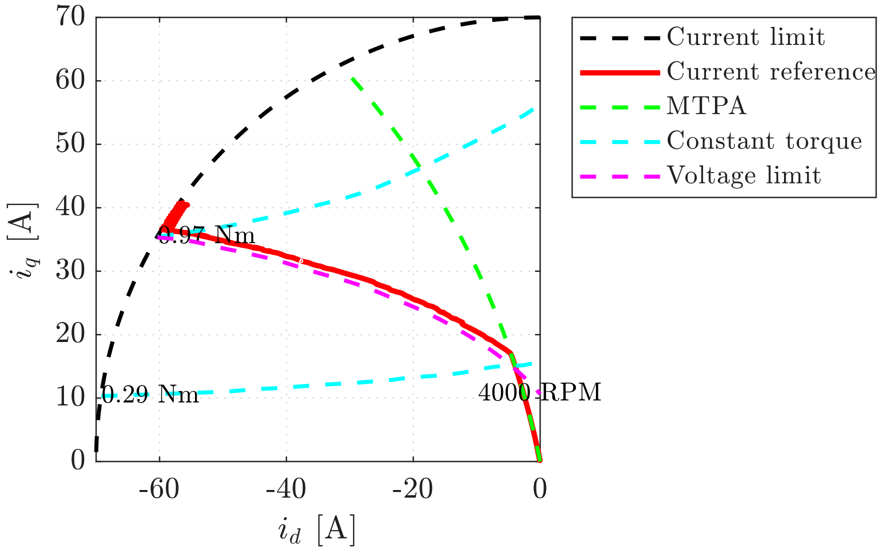

Figure 5.28: Current reference trajectory for case 2.

In the third test case, voltage limitation is further investigated. The load torque is held constant, while the speed reference is ramped up. The dynamic behaviour is shown in Figure 5.29.

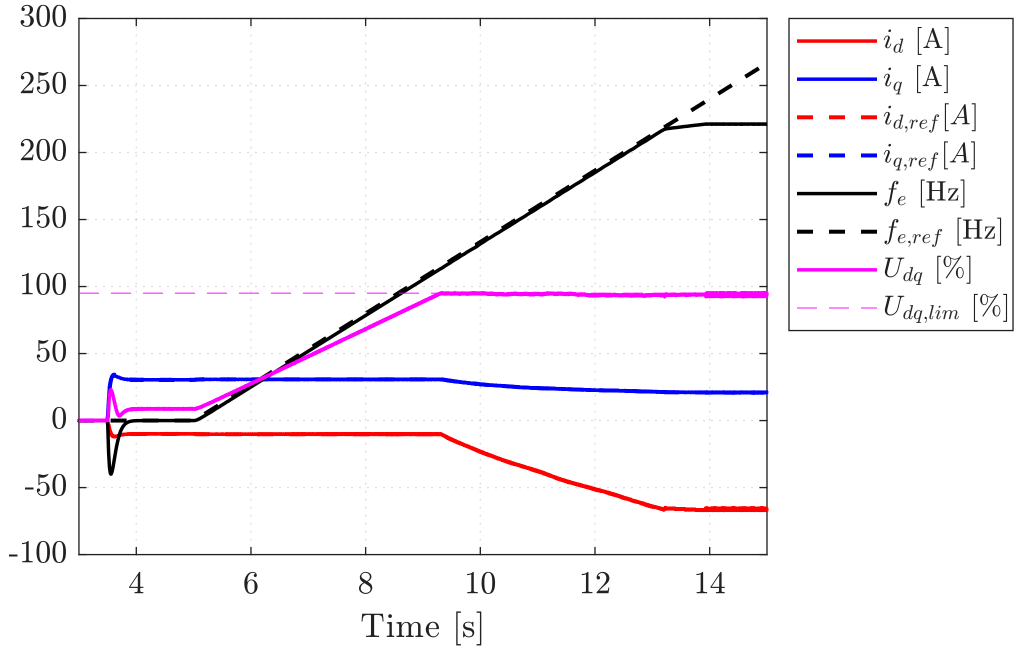

Figure 5.29: Dynamic performance for test case 3.

The dynamic performance shows the current increase as the constant load torque of 0.6 Nm is applied before 4 s. As the speed ramp begins at 5 s, the currents remain constant until the voltage limitation is reached shortly after 9 s. The speed continues to increase until approximately 11 s, where the currents and speed both flatten.

In Figure 5.30, the current reference trajectory is presented, as well as the voltage limit ellipses for 3330 and 6480 RPM and the constant torque curve for 0.6 Nm. As the constant load torque is applied, the current references increase along the MTPA trajectory. The current remains approximately constant at MTPA until the voltage limitation is reached and field weakening is applied. The current reference is shifted along the constant torque curve for the load torque of 0.6 Nm as the speed increases and field weakening deepens. When the current limit circle is reached, the speed can no longer increase while maintaining the load.

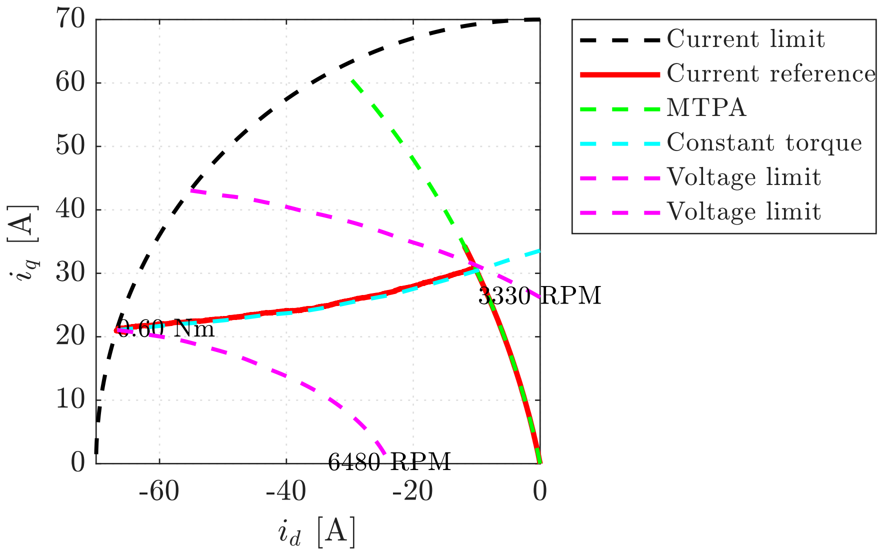

Figure 5.30: Current reference trajectory for case 3.

In the final test case, the behaviour under simultaneous voltage and current limitation is investigated. The results for the dynamic performance are illustrated in Figure 5.31. Initially, a load step of 0.4 Nm is applied and held constant, causing an increase in current. At 4 s, a speed step of 6000 RPM is applied, resulting in an additional rapid increase in the currents.

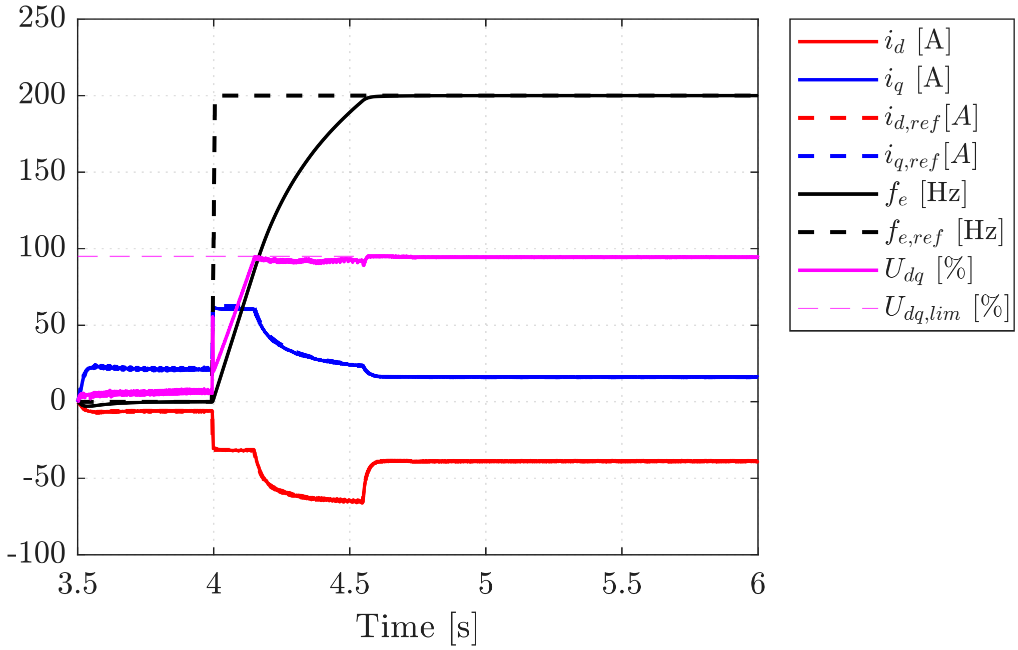

Figure 5.31: Dynamic performance for test case 4.

In Figure 5.32, the current references, voltage limit ellipse for 6000 RPM and the constant torque curve for 0.4 Nm are presented. The currents increase along MTPA for the initial load step. As the torque demand increases rapidly with the application of the speed step, the current references moves quickly along the MTPA, reaching the current limit circle in a few steps. As the speed closes on its reference value, the torque demand decreases and the current references shifts down the current limit circle, reducing torque and deepening the field weakening. As the speed reference is reached, the current references move along the 6000 RPM voltage limit ellipse reducing the current magnitude until the ellipse intersects the constant torque curve of 0.4 Nm.

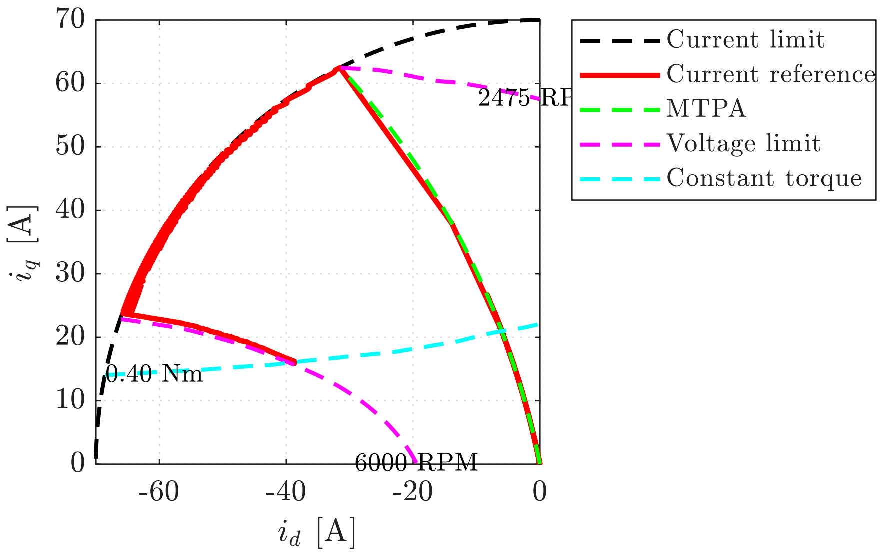

Figure 5.32: Current reference trajectory for case 4.

6

Discussion

6.1 Torque maps and MTPA trajectories

The torque contours in Figure 5.1 are asymmetric in the current plane, which is expected for a salient-pole machine, where $L_q > L_d$. This confirms that the reluctance torque component contributes significantly to the total torque, which shifts the MTPA trajectory into the second quadrant, $\beta > 90°$.

An important observation in the measured data is the shift of the zero-torque contour. In an ideal, linear machine model without any losses, the zero-torque curve lies on the d-axis. However, the mappings show that a small positive q-axis current is required to reach a zero torque reading on the torque sensor. This deviation is due to the mechanical losses of the machine and the test bench, as well as the iron losses of the machine. To overcome the friction of the shaft bearings and the iron losses induced by the permanent magnet flux rotating through the stator core, the machine must produce a torque to equal these losses.

The difference map between the mappings at 500 and 2000 RPM in Figure 5.2, shows a systematic reduction in torque production as rotational speed increases. This reduction is likely caused by speed dependent mechanical and iron losses. The iron loss speed dependence can be seen in (2.47) where all terms are dependent on the frequency, while the second term has a quadratic frequency dependence. The lower torque loss in the field weakening region of the left half plane indicate iron losses, since an injected negative d-axis current reduces the air gap flux, which in turn reduces the flux dependent iron losses.

The temperature difference map in Figure 5.3 shows the consequences of a stator temperature increase from 50 to 90 °C. The map shows a reduction in torque for higher temperatures. The two main temperature dependent machine parameters studied in this work are the stator resistance R_s and the permanent magnet flux linkage Ψ_m. The stator resistance increases with temperature, but does not meaningfully affect the torque production for a given current vector. This is due to the current controllers in the cascade control structure, that increase the modulated voltage as the resistance increases in order to keep the currents at their reference values. However, the reduction of the permanent magnet flux linkage, as described in Section 2.5.3, does reduce the produced torque for a given current magnitude.

The reduction in produced torque is increasing significantly for higher magnitudes of the q-axis current component. This further indicates the role of the reduced permanent magnet flux linkage since only the q-axis current component produces torque dependent on Ψ_m. This distribution in the current plane suggests that the reluctance torque component is mostly unaffected by the increase in temperature.

The comparison of the mapped MTPA trajectories in Figure 5.4 shows that, with the accuracy achieved in the measurements, it is difficult to reliably observe any meaningful shifts between the trajectories in the current plane. However, in Figure 5.5, the torque as a function of the current magnitude along MTPA shows a significant difference between the linear model and the mappings. The torque from the linear model is slightly convex, which becomes noticeable for higher current magnitudes where the increase in torque is faster, which is not present in the measured data. This super-linearity appears as the current angle increases toward 45°, where the reluctance torque component starts to increase quadratically with current magnitude. This effect should be present in the measured data, but is likely counteracted by magnetic saturation effects, that for higher current magnitudes reduce the produced torque for a given current magnitude.

These effects are more clear in Figure 5.6, where the torque per unit current is presented as a function of the current magnitude. This torque constant slowly increases with current, indicating a super linear torque trend for lower current magnitudes. For high current magnitudes, the torque constant stops increasing in the measured data, while continuing to grow in the linear model case.

Comparing the linear model to the mapped machine cases, the torque constants of the mapped machine is slightly higher for low temperatures and slightly lower for high temperatures compared to the linear machine model. Based on the torque constant values presented in Section 5.1 for the region 30 A to 40 A, where the torque is high enough to get decent accuracy of the torque constant while the machine is not saturated, percentage deviations can be determined. In this interval, the torque constant of the mapped machine at 50 °C is on average 0.65 % higher at 500 RPM and 0.50 % higher at 2000 RPM than the linear model constant. At the higher temperature of 90 °C, the torque constants are on average 0.94 % lower at 500 RPM and 0.22 % lower at 2000 RPM compared to the linear model. For higher currents, the torque constant continues to increase for the linear model, reaching 0.0209 Nm/A at 70 A while the mapped machine stops increasing at 0.0195 Nm/A for 50 °C and 0.0193 Nm/A for 90 °C due to magnetic saturation.

6.2 Flux linkage and inductance characteristics

The d- and q-axis flux linkage maps presented in Figure 5.7 and 5.8 show the shift from a linear state at low current magnitudes, to a non-linear and saturated state for higher currents magnitudes. In the linear regions, the coupling between the axes is small, as indicated by the straight and evenly spaced ISO-curves. However, as current magnitudes increase, two different saturation effects occur.

Firstly, the increase in ISO-curve spacing at high positive currents, as well as the decrease in L_d and L_q shown in Figure 5.13 and 5.14, indicate that the iron core is experiencing magnetic saturation, limiting the maximum flux density. Notably, the d-axis flux linkage saturates asymmetrically. For positive i_d currents, the flux created by the stator current helps the permanent magnet flux, saturating the iron core. However, for negative d-axis currents, as used in field weakening, the stator field opposes and weakens the permanent magnets. This keeps the total flux density low and prevents saturation, which explains why L_d remains approximately constant for negative d-axis currents. Comparing to the linear model parameters presented in Table 2.1 to the measured values, the linear model is within 5.0 % of the measured L_d for negative i_d and values of i_q below 30 A. For positive values of i_d, the measured value of L_d decreases to less than 50 % of the linear model value. The measured value of L_q is up to 13.7 % larger than the linear model value for low values of i_q and up to 60.2 % lower for $i_q = 70$ A. The linear model thus has to make a trade-off regarding where it needs to be the most accurate, in our case it is around $i_q = 20$ A and for $i_d < 20$ A.

Secondly, the clear bending of the ISO-curves when the orthogonal current component is high, suggest the presence of cross saturation. Because of this, at high d-axis currents, the q-axis current is not able to produce the same flux linkage in the q-direction, as when the d-axis current is low, and vice versa. The cross saturation is also visible in Figure 5.13 and 5.14, where increase in the orthogonal current component causes the inductances to decrease. The cross inductances, L_{dq} and L_{qd} shown in Figure 5.15 and 5.16, give another way of modelling the effects of cross saturation that the linear model does not include or assumes to be zero. Similarly to L_d and L_q, the measured cross inductances vary in the dq-plane. For the measured current vectors L_{dq} vary from -0.04 mH to 0.02 mH and L_{qd} vary from 0.03 mH to -0.03 mH, hence modelling them as zero is in the range but does not capture the complete dynamics of the system.

The speed difference maps for the flux linkages between 500 and 2000 RPM in Figure 5.9 and 5.10 suggests a speed dependence that differs from the linear model. Theoretically, the flux linkage should be speed independent. The clear activity around the origin of the current plane indicate a coupling between speed and the way the flux linkages are calculated from the data. Since the flux linkages are calculated from the voltage equations (2.17) and (2.18), any deviations in the measured voltages directly transfers to the flux deviation maps. At the lower speed of 500 RPM, the measured voltage magnitude is small, especially at the low current magnitudes around the origin of the current plane. Because of this, unwanted contributions from inverter dead time and transistor voltage drop among others, could have a significant impact on the voltage measurement. Additionally, small errors in the temperature compensation of R_s would affect the resistive voltage drop, and thereby, the calculated flux linkages. At 2000 RPM, these unwanted contributions are smaller compared to the back-EMF, resulting in more reliable calculation of the flux linkages. This difference between the cases of 500 and 2000 RPM could be a reason for the effects seen in the deviation maps. Furthermore, the higher deviation observed at positive d-current compared to negative d-currents could be caused by varying iron losses. Positive

d-axis currents increase the flux density and the iron losses at 2000 RPM.

The temperature deviation maps for the flux linkages are presented in Figures 5.11 and 5.12. The deviation maps compare the cases of 50 °C and 90 °C at 2000 RPM and show some dependence on temperature, especially in the d-axis flux linkage. For the d-axis flux linkage, the deviation is largest in the left half plane where i_d is negative. This reduction is likely caused by the reduction in the permanent magnet flux linkage as temperatures increase, as seen in Table 5.1. However, in the right half plane the reduction is significantly smaller. One possible explanation for this is that the machine only experiences magnetic saturation in the d-axis for positive d-axis currents. Since the machine is saturated in the d-axis in the right half plane, the reduction in permanent magnet flux linkage, and thus reduction in saturation level, at higher temperatures allow the applied positive i_d current to provide more flux linkage. This effect could counteract the effects of the reduced permanent magnet flux linkage. The q-axis flux linkage show less dependence on temperature, with a significantly smaller deviation across the current plane. The slight increase in q-axis flux linkage with temperature is possibly caused by reduced cross saturation from the d-axis due to the reduction in permanent magnet flux linkage.

The measurements of the stator resistance and permanent magnet flux linkage showed that R_s increased and Ψ_m decreased with temperature as expected. However, the calculated temperature coefficients from the measurements were lower than the theoretical thermal coefficients of resistance in copper and flux density of NdFeB magnets presented in Section 2.5.3. This can likely be explained by the fact that only the stator windings were directly temperature controlled, since the temperature sensor was located there. As the copper losses in the stator windings were the dominant source of heat generation, the winding temperature was probably higher than the temperature of the rest of the machine. The smaller measured increase in stator resistance may also be partly caused by the resistance of the cables, connectors, and inverter connections included in the measurement path. These parts were not heated in the same way as the windings and therefore contributed a resistance that was less dependent on the measured winding temperature. This indicates that estimating the resistance at different temperatures using only one resistance measurement and the theoretical temperature coefficient of copper may lead to less accurate flux linkage calculations. Similarly, the smaller measured decrease in Ψ_m compared to theory is likely explained by the rotor, where the permanent magnets are located, not reaching the same temperature as the stator windings. Although this means that the machine was not heated uniformly, comparisons between measurements at different stator temperatures should still be valid, since the machine was allowed to reach a repeatable thermal steady state before each measurement, as described in Section 3.2.2.

6.3 Voltage constraints in the current plane

The voltage limit ellipses presented in Figure 5.18 illustrate how the available operating region in the current plane shrinks as a function of speed for a given voltage limit due to the growth of the back-EMF. Interestingly, the ellipses calculated from the low speed mappings seem to be smaller, and thereby more limiting. This is not expected, since losses tend to increase with higher speeds, increasing the voltage demand. One possible cause is the higher relative voltage drop in the inverter compared to the absolute voltage levels at low speeds such as 500 RPM.

The voltage limit ellipse that lies on the edge of the current limit circle is at a speed of approximately 2400 RPM for the DC-link voltage of 12 V. Hence, for speeds above that, all current vectors within the current limit would not be reachable and the proposed sweep of current references would not be possible. This is one of the factors limiting the speed at which the mappings were performed, the other one being the DC current limitation of the power supply.

The linear model voltage ellipses follow similar paths as the mapped counterparts for high calculated speeds. For the cases of 2500 and 3000 RPM however, there is a large difference. Due to magnetic saturation and the drop in the inductances, the flux linkages increases more slowly than predicted by the linear model for increasing currents. This reduces voltage drop for a given current, meaning that the mapped ellipses become larger and less limiting than the linear model predicts. This is significant as it is a case where mapped data could provide a considerable improvement in voltage utilization compared to using the linear machine model.

The voltage ellipses calculated from the mappings at different temperatures in Figure 5.19 show different behaviour in different parts of the current plane and for varying speeds. For the case of low temperature, 50 °C, the permanent magnet flux linkage Ψ_m is relatively large, while the stator winding resistance R_s is small compared to the case of 90 °C. This causes the low temperature case to be more limiting at higher speeds, where the Ψ_m-dependent back-EMF voltage is more significant. At lower speeds, where the back-EMF is smaller, the increase in R_s causes a more noticeable increase in voltage drop, making the 90 °C case more voltage limiting.

With the drive system limits and the available DC supply voltage of 12 V, MTPV control is not applicable without overloading the system. If an inverter with higher current capabilities was used, the MTPV trajectory could have been reached.

6.4 Efficiency mapping and optimal trajectories

An interesting finding in the baseline case efficiency in Figure 5.20 is that the maximum measured efficiency peaks at approximately 65 %. For a modern PMSM, this efficiency value is low. One possible cause for this could be the presence of an uncompensated friction within the test bench.

Given the drive system limitations and the small physical size of the tested machine, the absolute torque values are small. Consequently, the calculation is very sensitive to even small static torque offsets. For example, adding a small torque offset compensation would increase the overall efficiency of the machine significantly. While a uniform offset shifts the absolute efficiency values, it does not change the distribution of the efficiency contours in the current plane. Because of this, the comparison between speed and temperature cases remains valid.

The speed deviation map in Figure 5.21 demonstrates an increase in efficiency of up to 30 percentage points when the speed is increased from 500 to 2000 RPM. This is a consequence of how the output power scales relative to the machine losses. The mechanical output power increases linearly with speed for a given torque. At 500 RPM, the mechanical output power is low, meaning that the speed independent copper losses and potential static friction components consume a large portion of the input power, reducing efficiency. When the speed is quadrupled to 2000 RPM, the mechanical power increases by a factor of four. Even though the speed dependent iron- and friction losses increase at 2000 RPM, their growth is small compared to the rate of the mechanical power increase within this speed region. This changes the loss to power ratio in favour of machine efficiency, especially in the high torque regions. At speeds considerably higher than the ones measured, there would likely come a point where iron losses became dominant, leading to a reduction of efficiency for higher rotational speeds.

The temperature difference map in Figure 5.22 demonstrates a reduction in efficiency across the entire current plane as the machine temperature increases. The maximum efficiency drop occurs close to the origin of the current plane. In this low current region, the mechanical output power is small. As temperatures increase and the stator resistance R_s grows, the resistive power loss increase instantly. Near the origin, even small absolute power increases in the copper losses make up a significant portion of the produced power, which reduces the calculated efficiency. At higher current magnitudes, the efficiency drop becomes smaller as the loss to power ratio becomes more favourable.

The trajectory comparison presented in Section 5.4.1 shows that there is little difference between the trajectories at the investigated operating conditions. The mean efficiency values presented in Table 5.2 show a slightly higher efficiency for MTPW, at 65.26 %, compared to the linear model MTPA at 65.22 % and mapped MTPA at 65.05 %. Notably, the linear model MTPA achieves higher mean efficiency than the mapped MTPA. This could be caused by the function fitted to the points not exactly representing the mapped MTPA points at each torque. Since these values are the averages of the efficiency at different torque levels, they only represent the true machine efficiency in applications where the entire machine torque range is used evenly. This relatively small difference between trajectories is expected from a loss contribution perspective. MTPW optimizes the total input power by minimizing the sum of all losses, including copper, iron and friction losses. MTPA only minimizes the stator current magnitude to reduce copper losses. Because the machine is operating within low to medium rotational speeds, the copper losses remain the dominant loss component. The speed dependent iron losses are not large enough to noticeably shift the MTPW trajectory relative to the MTPA trajectory. This close alignment validates the common approach of using MTPA for current reference selection, as it gives close to optimal efficiency with lower complexity. However, implementing MTPW does not cost anything in hardware, only in development time.

6.5 Data driven model and current selection

In section 5.5, the constructed machine model was compared to the mappings made at different speeds and temperatures. As expected, the model aligns closely with the measured data at 2000 RPM and 50 °C, from which its lookup-tables were generated. The error in torque for this case likely result mainly from the compensation of the zero-torque curve, performed to remove the measured test bench losses from the simulation model. The mean errors in the currents, amounting to < 0.5 A, are small and could be the result of the grid redistribution and interpolation in the machine model not intersecting the measured points exactly. One possible explanation for the large maximum current errors is sensitivity to small discrepancies in the grid and interpolations in areas with low voltage values and high currents, such as at high negative d-axis currents. As expected, the model had higher errors compared to the mappings performed at operating conditions further from 2000 RPM and 50 °C, reaching mean current errors above 3 A and a mean torque error of 0.141 Nm. This shows that the implementation of temperature and speed compensations in the machine model could be beneficial if the operating range of interest is wide.

The results from the simulations presented in Section 5.6 show the behaviour of the data driven current selector in different scenarios. The LUT-based approach manages to accurately follow the MTPA trajectory during operation without voltage limitations. When voltage limitations are present and field weakening is needed, the current reference selector can follow either constant torque curves to maintain a constant torque at increasing speed, or voltage limit ellipses to meet an increasing torque demand at a constant high speed. For the fourth case, presented in Figure 5.31, the current selection method also handles a scenario of max torque operation while increasing in speed, meaning both voltage and current limitations are acting at the same time. During operation in voltage limitation, the voltage utilization is held accurately at 95 %, as limited by the control implementation.

The implementation of the current vector selector suffers from slight numerical instability when shifting along the current limit circle, as apparent by the jagged reference trajectory in Figure 5.32. It also lacks feedback regarding the actual voltage utilization, making the method sensitive to model errors. This issue could possibly be resolved by implementing an external feedback regulator that fine-tunes voltage utilization after the LUT-based references have been applied. This could be used to ensure that the current references can be met while the voltage utilization is as high as possible despite potential model errors.

7

Conclusion

This thesis has investigated the characterization of a salient-pole PMSM, by the means of an automated mapping system. The automated mapping system allows for dataset collection at different speeds and temperatures, capturing the machine properties over a range of operating regions. Finally, a data-driven method for current vector selection in control was investigated in simulation.

The data collected from the mappings has provided several interesting insights into the behaviour of the machine and highlighted how it differs from the linear model. The largest deviations from the linear model could be explained by magnetic saturation and cross saturation at large current magnitudes. Within the investigated operating region, the calculated inductances based on the measurements showed that the values of L_d and L_q could vary up to 50 % and 60 % respectively compared to the linear model, while the cross inductances L_{dq} and L_{qd} had absolute values up to 0.04 mH and 0.03 mH respectively. These effects were especially noticeable in the linear model voltage ellipses compared to the ones derived from data, as well as calculated torque constants along the MTPA trajectory. In the unsaturated region of 30 A to 40 A, the mapped machine torque constants remained close to the linear model predictions, showing a maximum mean deviation of 0.000 120 Nm/A at 50 °C and −0.000 175 Nm/A at 90 °C, corresponding to 0.65 % and −0.94 % respectively. However, at high current magnitudes up to 70 A, magnetic saturation caused the mapped torque constants to stop increasing at 0.0195 Nm/A and 0.0193 Nm/A at low and high temperatures, deviating from the linear model torque constant that continued increasing up to 0.0209 Nm/A.

While speed dependent losses, like iron losses, could be noticeable, they did not have a significant impact at the speeds that were investigated in this work. When using the collected data to extract optimal current trajectories, based on either current magnitude or machine efficiency, the non-linear effects made a small difference. Across the entire machine torque range, the linear model MTPA achieved a mean efficiency of 65.22 %, the mapped MTPA 65.05 % and the mapped MTPW achieved 65.26 %. Hence, implementing MTPW would yield an efficiency increase of 0.04 percentage points compared to linear model MTPA or 0.21 percentage points compared to the mapped MTPA in this case. Since the implementation of MTPW does not involve any hardware costs, the development time may be worthwhile in certain applications, especially if iron losses are more significant.

Further the mapped data could be utilized to create a model for simulation that was used to evaluate control methods. Steady-state validations of the machine model against the collected datasets showed high model accuracy for the case used in table generation 2000 RPM and 50 °C, achieving mean current errors below 0.5 A and a mean torque error of 0.087 Nm, which can be largely attributed to the introduced zero-torque compensation. The accuracy of the model decreased when operating further from the generation conditions, with mean current errors above 3 A and a mean torque error of 0.141 Nm for the worst case of 500 RPM and 90 °C. The simulations performed on the investigated method for data-driven current vector selection indicated that it was a valid approach, handling several limitation cases effectively while the voltage utilization is held accurately at 95 %, as limited by the control implementation. Slight numerical instabilities were noted when operating along the current limit circle, highlighting the need for further refinement of the method.

8

Future work

The findings presented in this thesis could be explored further in multiple directions in future work. To extend and improve the quality of the collected dataset, a few changes to the used equipment are suggested. Firstly, it would be beneficial to use a larger and more powerful machine. This would reduce the impact of unaccounted friction losses, providing more reliable absolute efficiency calculations. Additionally, an inverter with higher voltage and current limits would allow the machine to be pushed deeper into its non-linear regions, possibly highlighting more significant differences between the linear machine model and the mapped counterparts. Finally, A bidirectional power supply would allow experimental mapping in the third and fourth quadrants, avoiding the introduction of symmetry assumptions.

Regarding the mapping method, a variable spacing of the current reference points across the current plane would allow for higher resolution measurements in areas of interest, while the mapping time remain reasonable. This could, for example, be used to capture more accurate MTPA or MTPW trajectories.

For the data driven current selection, it would be of interest to implement an external voltage margin controller in addition to the look-up table based selections. This could possibly allow safe operation closer to full voltage utilization. Finally, the current selection method could be validated on a real machine.

Bibliography

[1] IEA 4E Electric Motor Systems Annex, “Policy brief #9: Electric motor systems: Why are they important?”, International Energy Agency 4E Technology Collaboration Programme, Dec. 18, 2025. Accessed: May 20, 2026. [Online]. Available: https://www.iea-4e.org/wp-content/uploads/2025/12/4E-Policy-Brief-EMSA-9-20251218.pdf.

[2] International Energy Agency, “Electricity 2026: Analysis and forecast to 2030”, International Energy Agency, 2026. Accessed: May 20, 2026. [Online]. Available: https://iea.blob.core.windows.net/assets/b73798cb-e452-42b9-9d8a-07542de7a041/Electricity_2026.pdf.

[3] H. Wang, X. Chen, X. Wang, and Z. Li, “Design optimization of pmsm for electric vehicles based on an intelligent surrogate model selection method”, in *2024 IEEE 7th International Electrical and Energy Conference (CIEEC)*, 2024, pp. 2133–2137. DOI: 10.1109/CIEEC60922.2024.10583097.

[4] S. F. Gebremariam and T. T. Wondie, “Comparative analysis of electric motor drives employed for propulsion purpose of battery electric vehicle (BEV) systems”, *International Journal of Science and Research Archive*, vol. 10, no. 2, pp. 1097–1112, 2023. DOI: 10.30574/ijsra.2023.10.2.1074. Accessed: May 20, 2026. [Online]. Available: https://ijsra.net/sites/default/files/fulltext_pdf/IJSRA-2023-1074.pdf.

[5] R. Krishnan, *Permanent Magnet Synchronous and Brushless DC Motor Drives.* CRC Press, 2010, ISBN: 9781420014235.

[6] N. Bianchi, P. G. Carlet, L. Cinti, and L. Ortombina, “A review about flux-weakening operating limits and control techniques for synchronous motor drives”, *Energies*, vol. 15, no. 5, p. 1930, 2022. DOI: 10.3390/en15051930.

[7] J.-W. Jung, V. Q. Leu, T. D. Do, E.-K. Kim, and H. H. Choi, “Adaptive pid speed control design for permanent magnet synchronous motor drives”, *IEEE Transactions on Power Electronics*, vol. 30, no. 2, pp. 900–908, 2015. DOI: 10.1109/TPEL.2014.2311462.

[8] D. K. Cheng, *Field and Wave Electromagnetics*, 2nd ed. Pearson, 2013, ISBN: 9781292026565.

[9] L. Harnefors, *Control of power electronic converters and variable-speed drives*, 2005.

[10] WEG, *The abc's of synchronous motors*, WEG Electric Corp. Accessed: May 26, 2026. [Online]. Available: `https://static.weg.net/medias/downloadcenter/hfe/hf4/WEG-the-abcs-of-synchronous-motors-usaem200syn42-brochure-english.pdf`.

[11] D. Reney, "Modeling and simulation of space vector PWM inverter", in *2011 International Conference on Devices and Communications (ICDeCom)*, IEEE, 2011. DOI: `10.1109/ICDECOM.2011.5738466`. Accessed: May 26, 2026. [Online]. Available: `https://ieeexplore.ieee.org/document/5738466`.

[12] N. Mohan, T. M. Undeland, and W. P. Robbins, *Power Electronics: Converters, Applications, and Design*, 3rd. Hoboken, NJ: John Wiley & Sons, Inc., 2003.

[13] C. Nordling and J. Österman, *Physics Handbook: For Science and Engineering*, 9th. Lund, Sweden: Studentlitteratur AB, 2020, ISBN: 9789144128061.

[14] W. Rodewald, M. Katter, B. Wall, R. Blank, G. Reppel, and H. Zilg, "Dependence of the coercivity h/sub cj/ of high energy nd-fe-b magnets on the alignment coefficient", *IEEE Transactions on Magnetics*, vol. 36, no. 5, pp. 3279–3281, 2000. DOI: `10.1109/20.908769`.

[15] R. Ni, D. Xu, G. Wang, L. Ding, G. Zhang, and L. Qu, "Maximum efficiency per ampere control of permanent-magnet synchronous machines", *IEEE Transactions on Industrial Electronics*, vol. 62, no. 4, pp. 2135–2143, 2015. DOI: `10.1109/TIE.2014.2354238`.

[16] Python Software Foundation. "Threading — thread-based parallelism". Python 3 documentation, Accessed: Jun. 1, 2026. [Online]. Available: `https://docs.python.org/3/library/threading.html`.

[17] The SciPy Community, *RBFInterpolator – SciPy v1.17.0 Manual*, SciPy, 2026. Accessed: May 31, 2026. [Online]. Available: `https://docs.scipy.org/doc/scipy/reference/generated/scipy.interpolate.RBFInterpolator.html`.

DEPARTMENT OF ELECTRICAL ENGINEERING
CHALMERS UNIVERSITY OF TECHNOLOGY
Gothenburg, Sweden
www.chalmers.se

CHALMERS
UNIVERSITY OF TECHNOLOGY